

Air-Stable Li_xAl Foil as Free-Standing Electrode with Improved Electrochemical Ductility by Shot-Peening Treatment

Huimin Fan, Sa Li,* Yue Yu, Hui Xu, Mengwen Jiang, Yunhui Huang, and Ju Li

A self-supporting Al foil anode should be attractive to the lithium-ion battery (LIB) industry. However, initial attempts at using thin Al foil directly as a LIB anode ends up with extremely large initial Coulombic inefficiency and gross mechanical failures in just a few cycles. This feels incongruent with the expectation that face-centered cubic Al should have good ductility. In this study, the discrepancy between “electrochemical ductility” and “mechanical ductility” is explained. Unlike “mechanical ductility” based on dislocation slip inside each grain, here it is proposed that “electrochemical ductility” of such high-capacity alloy foil electrodes should be related to grain boundaries (GB) activities. It is found that after reducing the grain size $D > 50 \mu\text{m}$ of the starting Al foil by shot-peening treatment, higher GB density (e.g., smaller initial grain size $D < 20 \mu\text{m}$) greatly alleviates the initial porosity damage after the roll-to-roll mechanical prelithiation and significantly improves electrochemical ductility thereafter, with enhanced cycle life in various kinds of full cells. Li_xAl foil also demonstrates surprising air stability with negligible capacity loss even after several hours' exposure to air. Such thin prelithiated metallic foil anodes are therefore highly competitive against pure Li metal foils.

results,^[4,5] plagued by the very low initial Coulombic efficiency (ICE) and catastrophic failures, which originate from the transformation stress and damage accumulation during lithiation/delithiation. Recently, a mechanical prelithiation (MP) approach has been shown to improve the low ICE and increase the electrochemically extractable Li inventory (LiInv) of alloy foil anodes in practical full cells.^[6,7] However, direct MP on well-annealed, commercial Al foils does not give as good results as other metal foils like Sn foils.^[8,9]

Face-centered cubic (FCC) aluminum, with relatively low melting temperature of $T_M = 933.5 \text{ K}$, should be *better* prepared to absorb the mechanical and electrochemical shocks among just the *high-capacity* anode materials, e.g., compared to *silicon*.^[10] But prior experiments did not bear out such intuition, as the Al foil behavior is often even worse than

silicon powders. Careful inspection in metallic foil electrodes reveals that this intuition of equating “mechanical ductility” with “electrochemical ductility” is often counterproductive. For example, grain refinement treatments usually lead to higher strength (Hall–Petch relation) but poorer mechanical ductility, i.e., the well-known mechanical strength–ductility tradeoff. But we very often find that smaller-grain-sized Al foils, with clearly poorer mechanical ductility than coarse-grained Al foils, actually show much better abilities to tolerate the MP shock and subsequent electrochemical cycling, i.e., showing better electrochemical ductility in practice, all at room temperature.^[7,11] Actually, we now think the right comparison should not be between aluminum and silicon, but should be between aluminum (particularly its GB regions) with the polymeric binders used in holding the silicon powders together in electrodes.

“Ductility” is defined here as the ability of a material to acclimate to certain stimuli (mechanical, electrochemical, etc.) without wholesale electrical or mechanical failures. These failures are often triggered by gross geometric deformation and topology changes, e.g., an originally contiguous metallic foil that fragments into many topologically disconnected pieces when Al_{FCC} (lattice parameter 4.05 \AA) is lithiated to form LiAl_{B32} phase with Zintl-phase NaTl (B32) atomic structure (lattice parameter 6.37 \AA , see **Figure 1A**). As a result, the foil loses electrical percolation and/or mechanical load-bearing capability, two functions of the conventional copper current collector plus slurry coating in LIBs. While the requirement to maintain


1. Introduction

Intuitively Al foil should be used as a favorable lithium-ion battery (LIB) anode, considering its high theoretical gravimetric capacity of $\text{Al} \rightarrow \text{Li}_9\text{Al}_4$ (2235 mAh g^{-1}),^[1,2] appropriate electrochemical potential plateau ($\approx 0.2\text{--}0.45 \text{ V vs Li}^+/\text{Li}$) that does not precipitate out Li_{BCC} phase, low cost, good electrical conductivity, and the fact that one no longer needs the expensive and very heavy Cu current collector.^[3] Yet, historical attempts at using Al foil anode in LIB full cells showed very pessimistic

H. Fan, Prof. S. Li, Y. Yu, Dr. H. Xu, M. Jiang, Prof. Y. Huang
School of Materials Science and Engineering
Tongji University
Shanghai 201804, China
E-mail: lisa@tongji.edu.cn

H. Fan, Prof. S. Li, Y. Yu, Dr. H. Xu, M. Jiang, Prof. Y. Huang
Institute of New Energy for Vehicles
Tongji University
Shanghai 201804, China

Prof. J. Li
Department of Nuclear Science and Engineering
and Department of Materials Science and Engineering
Massachusetts Institute of Technology
Cambridge, MA 02139, USA

 The ORCID identification number(s) for the author(s) of this article can be found under <https://doi.org/10.1002/adfm.202100978>.

DOI: 10.1002/adfm.202100978

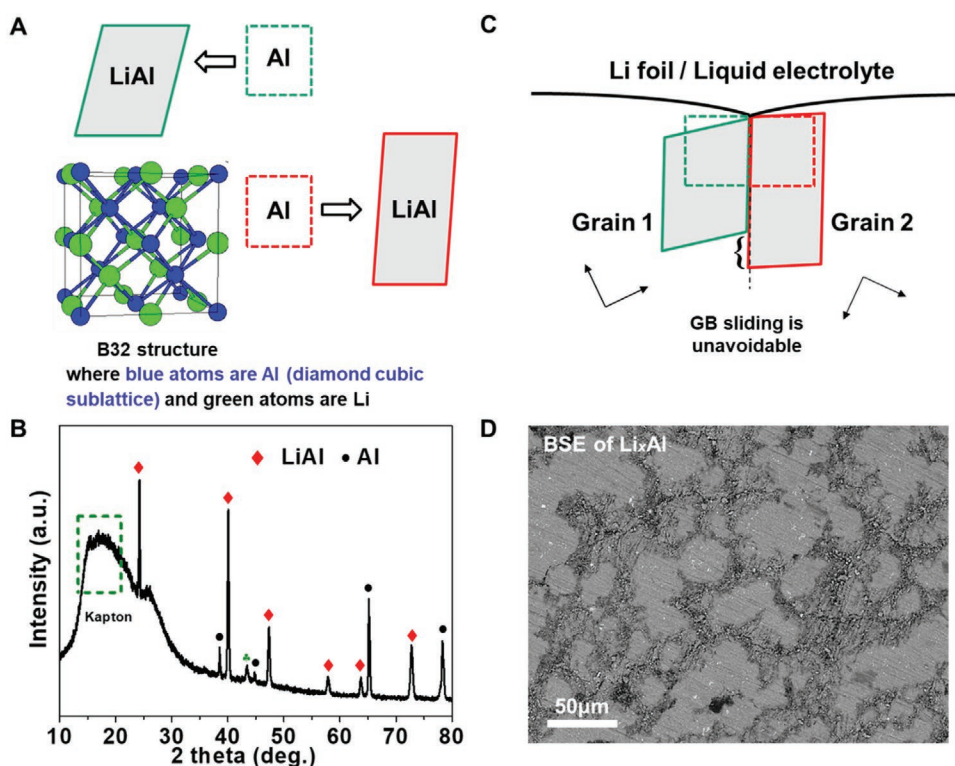


Figure 1. Illustration of extensive GB sliding upon first lithiation. A) shows how the green and red regions will phase-transform. Even though LiAl_{B32} has cubic symmetry, there has to be at least 1×2 Al lattice reconstruction to transform into diamond Al sublattice, so significant shear strain is likely involved. B) XRD pattern of the MPed Al foil: $\text{Al}_{\text{FCC}} \rightarrow \text{LiAl}_{\text{B32}}$ (green mark at 43.6° belongs to the XRD specimen stage). C) shows two adjacent FCC Al grains, with different crystallographic cube axes. The green and red boxes delineate regions to be lithiated. Note that they share an edge of equal length. Invasion of Li atom along the GB, which has much higher Li atom diffusivity at room-temperature than the bulk,^[15,16] and subsequent transport into the green and red boxes cause the transformations. Remember this is happening at room temperature, so fully civilian phase transformation is quite difficult. To maintain grain-to-grain adhesion, the two LiAl_{B32} parallelepipeds will try to rotate and maintain metallic contact along the original edges, but since the red region now has longer edge than the green region (i.e., the original GB is not an “invariant plane” of the transformation), there has to be GB sliding, illustrated as the displacement offset. Such sliding would preserve metallic contact. D) Backscattered electron (BSE) image of the Li_xAl sample at the Li invading front.

grain-to-grain adhesion and metallic contact without harming electron percolation is the same as in the mechanical ductility problem, for “electrochemical ductility” the $\text{Al}_{\text{FCC}} \rightarrow \text{LiAl}_{\text{B32}}$ (Figure 1B) reconstructive phase transformation brings about a different set of challenges, and not just the magnitude of the volume change. Actually, even though compressive hydrostatic stresses should be generated during MP, we find significant porosities on the order of 30 vol% were created right after MP (detail calculation can be found in Supporting Information note). This indicates likely geometric incompatibility. Note that while Al_{FCC} and LiAl_{B32} both have cubic lattice symmetry, the local lattice correspondence that connects Al_{FCC} to LiAl_{B32} may engender large shear strain,^[12] since at least 1×2 Al lattice reconstruction^[13] is needed to turn FCC (1 Al per primitive cell) into a diamondoid Al sublattice (2 Al per primitive cell). The lattice correspondence between the two cubic phases can never respect cubic symmetry (triaxial hydrostatic transformation), since suppose $m \times m \times m$ FCC Al transforms to $m' \times m' \times m'$ diamond cubic Al sublattice, conservation of Al atoms would require $m^3 = 2m'^3$, or $m = 2^{1/3}m'$, but such integer pairs m , m' can never be found. Therefore, symmetry breaking in one of the three axes, thus orientation variants (say two FCC cells along just one of three equivalent crystallographic axes

merge into one diamondoid), must be involved, and the stress-free transformation strain cannot be free of deviatoric component. While detailed atomistic calculations^[12,13] of such phase transformation need to be done, we can be sure of the above quantitative assessment. Remember this is happening at room temperature, so fully civilian phase transformation^[14] is quite difficult. This kind of shear-induced incompatibility would be the greatest at GBs, since two adjacent crystals are unlikely to have matching GB length after respective transformations, and GB sliding must be involved (Figure 1C).

Fundamentally, Al_{FCC} is mechanically ductile because external mechanical load is the stimulus and the internal stress is distributed rather uniformly inside the grain, and each Al_{FCC} grain has 12 $\{111\} \langle 110 \rangle$ slip systems that can respond to the stimulus facilely. Electrochemical ductility is rather different, the stimulus is the chemical invasion of Li atoms, which happens quite locally, first along the GBs (estimated to have diffusivity 4 orders of magnitude larger than bulk diffusivity at room temperature^[15,16]). Evidence of such GB-led transformations to the Zintl phase can be seen in Figure 1D, where the near-GB regions are heavily transformed at the Li invading front. The degree of the phase transformation is startling: $\approx 100\%$ volume change, with locally and globally large shear (deviatoric

strains as well. Once transformed, the product $\text{LiAl}_{\text{B}32}$ intermetallic phase is unlikely to further plastically deform much due to its larger Burgers vector. Therefore, electrochemical ductility hinges much more on GB motions (GB sliding and tendency of GB cracking). Good electrochemical ductility may be expected with *more prolific GB sliding systems* to relieve the stress, so less parasitic tensile stress is transmitted across GB that abets cracking. Also, a lot of small-length cracks, e.g., mother–daughter crack system, are much better than a major crack. This is a tried-and-true approach in ceramic toughening (see “Microcrack Toughening” in ref. [17]). Larger-grained Al foil has more risk to become electronically isolated by Weibull statistics argument due to the natural tendency to crack along pre-existing GB networks. Recall that the foil is tens of microns thick, so coarse-grained Al foil may have grains comparable to the foil thickness, and considering the electrolyte is like a corrosive liquid^[18] that prefers to etch along the grain boundaries, a coarse-grained foil with wide and deep cracks (see later, Figure 3E) cannot offer sufficient defense-in-depth to protect global electronic percolation as a very fine-grained foil (Figure 3G). In this work, we applied shot-peening treatment to pristine Al foil for enhancing electrochemical ductility by virtue of grain refinement, combined with a facile roll-to-roll MP to increase LiInv, making self-supporting Li_xAl foils with improved electrochemical ductility/endurance. In $\text{LiFePO}_4\|\text{S-Li}_x\text{Al}$ full-cell, it exhibits stable cycling for 100 cycles with 90% capacity retention. S- Li_xAl foils (about 110 μm thick) also show excellent compatibility with commercially available high voltage $\text{LiNi}_{0.5}\text{Co}_{0.2}\text{Mn}_{0.3}\text{O}_2$ (NCM523) cathodes for 160 cycles. The assembled $\text{LiCoO}_2\|\text{S-Li}_x\text{Al}$ pouch cells have 286 Wh kg^{-1} and 706 Wh L^{-1} energy density, and can be paired against sulfur (S_8) cathodes as well. Furthermore, the S- Li_xAl foil also demonstrates surprisingly robust air stability with negligible capacity loss even after several hours’ exposure to air.

2. Results and Discussion

Shot-peening, commonly used for extending the fatigue life of metals,^[19,20] is adopted before the metallurgical reaction shock of MP (Figure 3A). As illustrated in **Figure 2A,B** (pristine Al foil denoted as P-Al and shot-peening Al foil denoted as S-Al), when performing shot-peening treatment, the shot spheres continuously bombard the surface of the foil, causing dislocations to be created and rearranged and form denser grain boundary network. While increasing the shot-peening processing time and pressure helps further reduce the grain size, as revealed in previous reports,^[21,22] unfortunately, in this study, considering foil thickness is only $\approx 90\ \mu\text{m}$ (in a pursue of higher energy density), the Al foil was easy to get pierced when the pressure increased from 1.2 to 1.6 bar (Figure S1A, Supporting Information). Moreover, as the processing time rose from 5 to 20 s at the pressure of 1.2 bar, uniformly distributed indents could be observed on the S-Al foil, which is in sharp contrast to the flat surface of P-Al foil (Figure S1B,C, Supporting Information). Concomitantly, the surface roughness increased a lot (Figure S1D, Supporting Information) and damage occurred (Figure S1C, Supporting Information), which turns out to degrade electrochemical performance (Figure S1E, Supporting Information). As a compromise, the processing parameters of 1.2 bar pressure and 5 s were chosen here. From the electron backscattering diffraction (EBSD) in Figure 2C, grains both larger than 20 μm and smaller than 5 μm (marked by the white box) are observed in S-Al. In contrast, the as-purchased P-Al foil (Figure 2D and Figure S1F, Supporting Information) exhibited coarse grains with size even larger than 50 μm . Transmission electron microscopy (TEM) characterization is conducted on the fine grains smaller than 5 μm that are marked in Figure 2C. In comparison to the P-Al foil in Figure 2F, where a large view-field contains only scattered dislocations without signs of GB, in

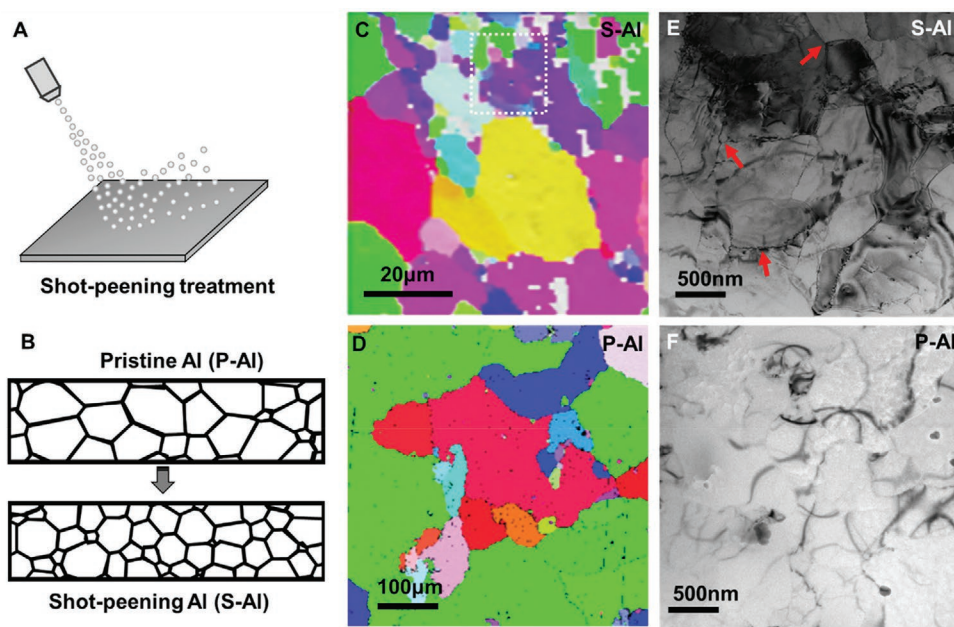


Figure 2. Sketches of shot-peening treatment process and characterizations of Al foils. A,B) Illustration of shot-peening treatment process. C,D) Inverse pole figure (IPF) map of EBSD data collected from C) S-Al foil and D) P-Al foil. E,F) TEM images of E) S-Al foil and F) P-Al foil.

S-Al sample some small grains and the GB network comprised of rearranged dislocation walls were observed (Figure 2E). X-ray diffraction (XRD) characterization (Figure S2, Supporting Information) revealed peak broadening due to the reduced grain size for S-Al, and we also note that the peak centroid shifted $\approx 0.15^\circ$ simultaneously, corresponding to -0.23% change in the lattice constant, meaning a residual compressive stress was generated on the surface. However, as the phase-transformation inelastic strain usually exceeds 50%, we think such initial compressive strain/stress cannot matter as much to the electrochemical ductility behavior as the effect of GB sliding.

A roll-to-roll MP process was subsequently applied to S-Al foils and P-Al foils (illustrated as Figure 3A), where a 50 μm thick Li foil (Figure S3A, Supporting Information) is sandwiched between two aluminum foils (each 93 μm thick), and then rolled by a rolling machine with 30 MPa pressure to get solid-state metallurgical reactions, as demonstrated in Figure S3B in the Supporting Information. XRD characterization after MP process in Figure 3B reveals the presence of LiAl_{B32} (JCPDS No. 65–3017) phase, without signs of “lithium-rich” phases such as Li_3Al_2 and Li_9Al_4 . From the cyclic voltammetry (CV) test shown in Figure 3C, two coupled redox peaks at the potential around 0.2 V and 0.5 V (vs Li^+/Li) corresponding to the formation and decomposition of LiAl_{B32} are observed, suggesting LiAl_{B32} is the dominant reaction product during room-temperature electrochemical lithiation as well. Besides, some residual Al can be detected, which is reasonable considering 25 μm thick Li (50 μm Li is equally shared by two pieces of Al foils) theoretically should consume only $\approx 20.47 \mu\text{m}$ thick Al, much less than the 93 μm original thickness of the Al foil (detailed calculation can be found in the Supporting Information note). Thus, when further electrochemically lithiating MPed Li_xAl to 0.05 V cut-off voltage, the Li_xAl disk showed a 19.54 mAh cm^{-2} further lithiation capacity (Figure 3D). On the other hand, $\approx 5 \text{mAh cm}^{-2}$ LiInv can be extracted if electrochemical delithiation was first conducted on the Li_xAl foil right after MP, as shown in Figure 3D, which indicates that the original Li content could be completely absorbed by the two Al foils without any residual lithium metal (Figure S4, Supporting Information), since 4.85 μm thick Li corresponds to 1 mAh cm^{-2} of LiInv and $25/4.85 \approx 5 \text{mAh cm}^{-2}$.^[23] For detailed microstructural observation, the Li_xAl foils were inspected by scanning electron microscope (SEM; the MPed P-Al is denoted as P- Li_xAl and the MPed S-Al is denoted as S- Li_xAl). For P- Li_xAl foil, because the pristine coarse-grained Al foil provided insufficient GBs for sliding to release the enormous stress, the geometric incompatibilities of phase transformation induced severe cracking, as shown in surface and cross-section SEM images (Figure 3E,F, respectively), where $\approx 10 \mu\text{m}$ wide cracks apparently spread all over the foil's top surface. In this case, during the following electrochemical cycling, the liquid electrolyte will penetrate into the opening, and liquid electrolyte decomposition and solid-electrolyte interphase (SEI)^[23] will further jack up the major crack and insulate it, bringing about serious damage. In contrast, Figure 3G,H show the neat and intact lithiated layer with negligible wide or deep cracks on the surface of S- Li_xAl foil, as well as much more compact structure in the cross-section. Certain kind of self-healing may be possible^[10] if the crack opening is not too wide.

To quantify such different initial lithiation shock, the porous reacted layer (Figure 3F,H) was carefully examined by computing the porosity/total “free volume” for S- Li_xAl and P- Li_xAl , respectively, based on mass conservation, the known lattice constants of phases, and the measured nominal thickness after MP. Detailed calculation (Supporting Information note) reveals that the P- Li_xAl has a huge amount of porosity, $p_{\text{P-Li}_x\text{Al}} = 13.2 \mu\text{m}/42.1 \mu\text{m} = 31.4 \text{vol}\%$, approaching that of slurry coatings in conventional LIBs (even though we profess to make a foil anode). In contrast, $p_{\text{S-Li}_x\text{Al}} = 9.25 \mu\text{m}/53.9 \mu\text{m} = 17.1 \text{vol}\%$, which is much less damaging mechanically and electrically, considering not all free volume belongs to open pores and much of the 17.1 vol% could be trapped inside the ultra-nanocrystalline LiAl/LiAl GBs, that facilitate Li GB diffusion but do not allow liquid electrolyte invasion.^[11] This demonstrates a much less severe initial MP damage for metal foils after the prior shot-peening treatment.

For further investigations into the underlying causes of this divergent initial damage, the forefront of Li-Al metallurgical reaction was examined by polishing down the top Li_xAl product layer and exposing the uppermost plane that lithium starts to invade. Careful SEM and backscattered electron (BSE) characterizations are demonstrated in Figure S5, Supporting Information, in which the lithiated area is apparently different from the unreacted Al. Notably, the corresponding BSE mode reveals the Li_xAl phase always prefers to gather on the closed-ring boundaries, leaving interior of the ring with residual Al_{FCC} phase, as revealed in Figure S5B,D in the Supporting Information. The size of those “tribes” is estimated to be 10–50 μm for S- Li_xAl and $>50 \mu\text{m}$ for P- Li_xAl , which agrees well with the original grain size (before MP) observed by EBSD (Figure 2C,D). That is to say, lithium diffusion into Al matrix mainly occurs at grain boundaries, the as-formed LiAl phase would also happen locally there due to the facile kinetics. Therefore, once MP starts, the transformed region would mainly rely on the GB activities, especially GB sliding (as illustrated in Figure 1A,C) to accommodate the out-of-plane anisotropic expansion and relieve stress. In a sense, the GBs in foil electrode play the same role as the binders and conductive agents in conventional LIB anodes, in that they are responsible for maintaining mechanical adhesion and electronic percolation despite the stresses that must be transmitted across them. The prolific, dense GB sliding system for S- Li_xAl (Figure 2C) would spontaneously distribute the huge stress evenly and thus contribute to the less-damaged electrode and robust electrochemical ductility, whereas for P-Al with sparse GBs, it would inevitably create wider and deeper cracks due to poor stress relaxation that result in the more porous and electrically isolated structure.

In order to carefully determine the impact of retained Al_{FCC} phase in Li_xAl anodes, a half cell was prepared by pairing it against 200 μm thick Li foil. When the S- $\text{Li}_x\text{Al}||\text{Li}$ half cell was first lithiated with 2.5 mAh cm^{-2} and then delithiated to 2.5 V at 1 mA cm^{-2} , it can be found that the lithiation voltage plateaus at $\approx 0.25 \text{V}$ and the delithiation voltage plateaus at $\approx 0.4 \text{V}$, which is exactly the same as the S-Al $||\text{Li}$ half cell (Figure S6A, Supporting Information), indicating the retained Al_{FCC} phase is still active in the same manner. The retained Al_{FCC} phase after MP acts as both current collector (support the free-standing structure) and active material. Especially, when there is abundant lithium

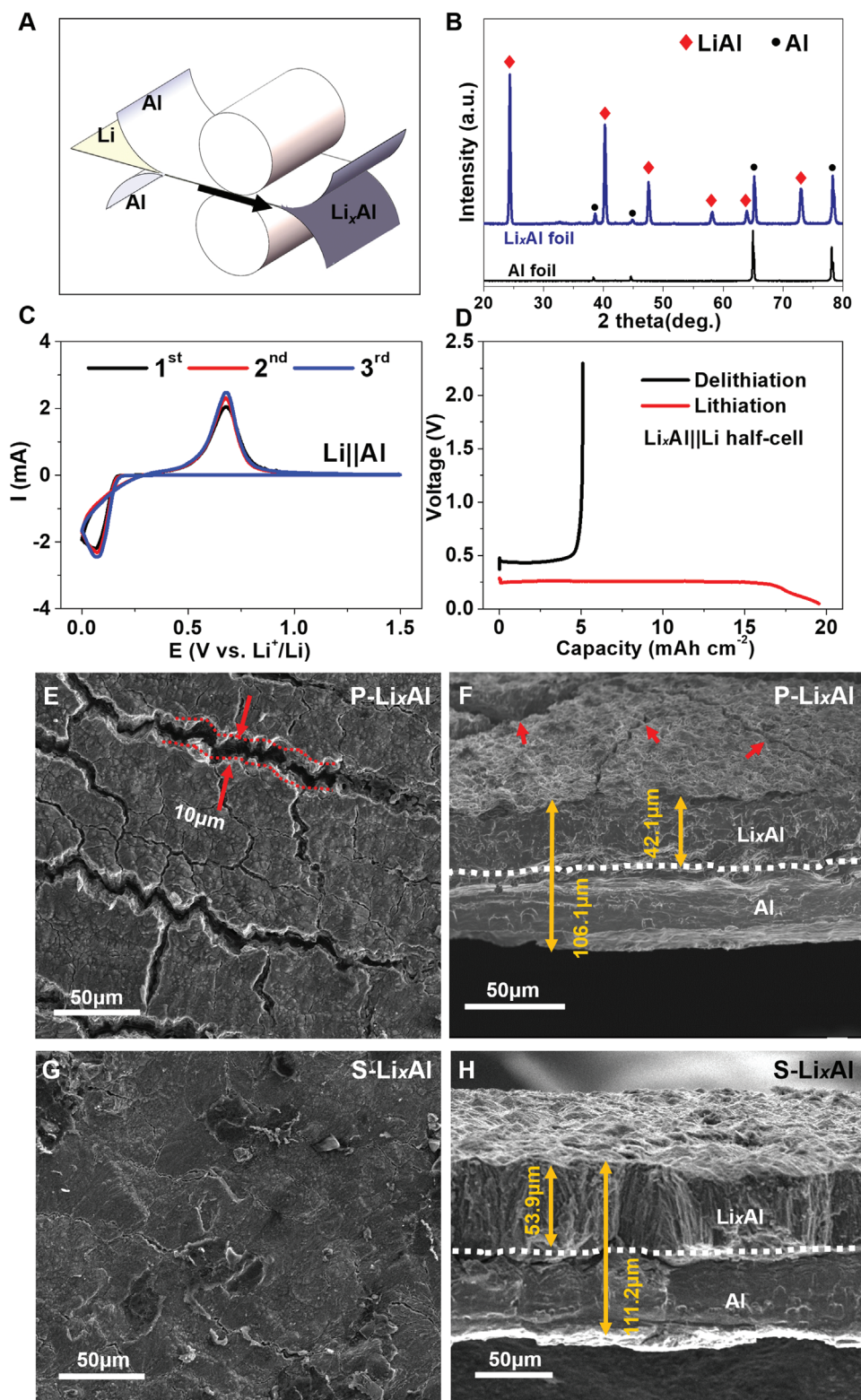


Figure 3. Schematic of industrial prelithiation production process, characterizations, and morphology analysis of as-obtained P-Li_xAl and S-Li_xAl. A) Schematic of industrial production process of roll-to-roll prelithiation of Al foil. B) XRD patterns of Li_xAl alloy foil after MP. C) Cyclic voltammetry curves of Al||Li half cell at scanning rate of 0.2 mV s⁻¹. D) Two separate experiments: the red line represents electrochemically lithiating the as-prepared Li_xAl foil to 0.05 V cut-off voltage and the black line represents electrochemically delithiating the as-prepared Li_xAl foil in half cell. E, F) SEM images of E) top-view and F) cross-section of the P-Li_xAl foil. G, H) SEM images of G) surface topography details and H) cross-section details of S-Li_xAl foil.

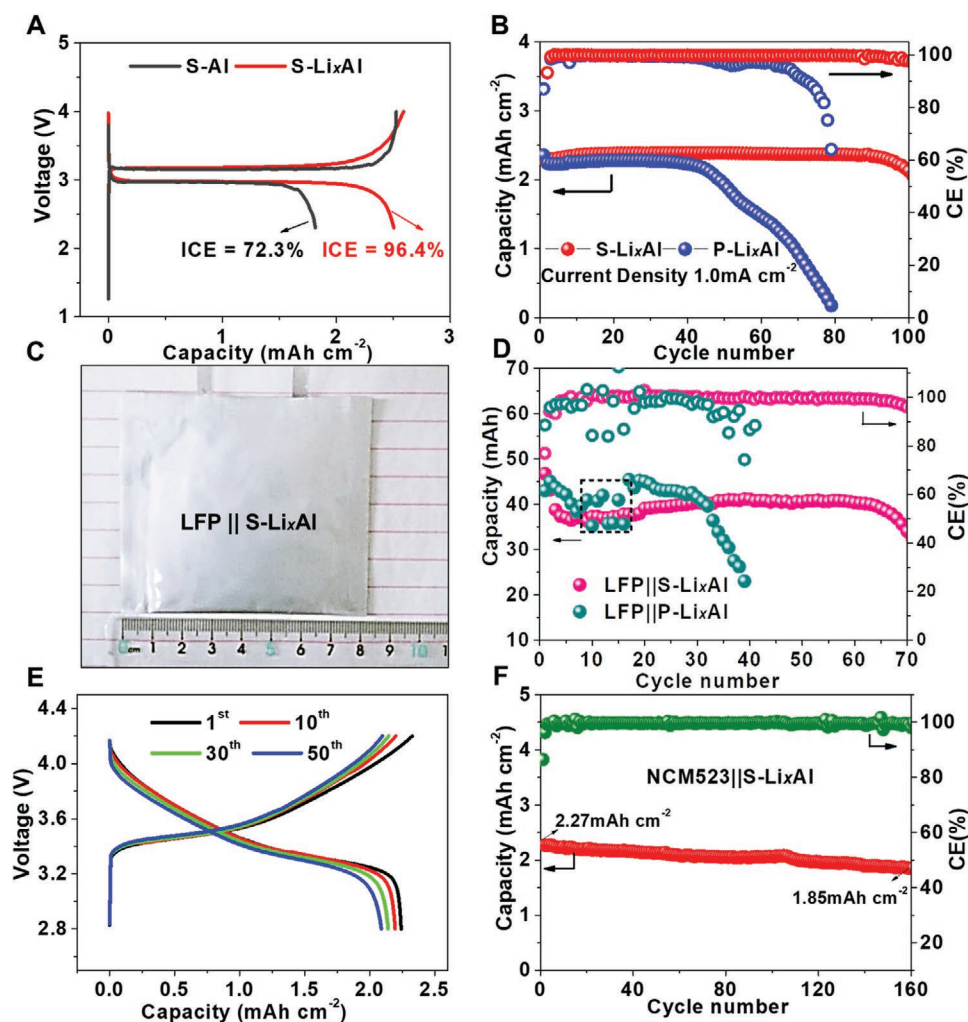


Figure 4. Full-cell battery performance of as-obtained S-Li_xAl foil. A) Initial galvanostatic charge–discharge curves of LFP||S-Li_xAl/S-Al full cells at 1 mA cm⁻² current density. B) Cycling performance comparison between P-Li_xAl and S-Li_xAl foil at 1 mA cm⁻² with LFP cathodes in full cells. C) Optical photo of LFP||S-Li_xAl pouch cell. D) Comparison of electrochemical performance in pouch cells (LFP||S-Li_xAl and LFP||P-Li_xAl). E) Voltage profiles and F) cycling performance of NCM||S-Li_xAl full cells with 2.4 mAh cm⁻² nominal capacity.

source in the counter electrode (the 200 μm thick Li foil), a stable cycling as long as ≈200 cycles is achieved (Figure S6B, Supporting Information). To further evaluate the advantages of shot-peened S-Li_xAl with limited LiInv, galvanostatic charge/discharge tests were performed with limited-electrolyte/LiInv full cells, by pairing as-obtained S-Li_xAl and P-Li_xAl foils against commercial LiFePO₄ (LFP) cathodes of areal capacity 2.65 mAh cm⁻². **Figure 4A** exhibits the initial voltage curves of the LFP||S-Li_xAl cells, whose ICE reaches 96.4%, demonstrating the significantly improved ICE after MP (from 72% of the Al foil to 96% of the Li_xAl foil), despite the existence of an alumina layer on the surface of Al foil which seems to have negligible impact (as demonstrated in Figure S6C, Supporting Information). Such improved ICE is ascribed to the pre-stored LiInv in S-Li_xAl, basically, within fixed full-cell voltage cutoffs [V_{upper} , V_{lower}], as well as decreased SEI creation (as characterized by X-ray photoelectron spectroscopy (XPS) in Figure S7, Supporting Information). From the voltage profiles for LFP||S-Li_xAl in Figure S8A in the Supporting Information,

typical Al-Li alloying/dealloying process with LFP cathode was detected at ≈3.0 and ≈3.1 V respectively, and the subtle voltage change during the cycling from the 1st to 90th indicated a steady cycling performance. The long-term electrochemical cycling performance with a current density of 1 mA cm⁻² is displayed in Figure 4B, in which the CE rises to 99.9% in the third cycle for the S-Li_xAl, and the discharge capacities remain stable at 2.4 mAh cm⁻², with 92.3% capacity retention even after 100 cycles. However, cells without shot-peening treatment before MP showed much worse ability to tolerate the electrochemical cycling, its CE kept below the S-Li_xAl and even lowered than 99.5%, then decayed rapidly after 40 cycles (Figure S8B, Supporting Information). Moreover, as the current rate increased to 2.5 mA cm⁻², S-Li_xAl foil maintained decent performance, with 92% capacity retention after 90 cycles, much improved compared with P-Li_xAl as shown in Figure S8C in the Supporting Information. Additionally, large-format pouch cells (Figure 3C) were fabricated to assess the practical feasibility of free-standing Li_xAl foil anode, by pairing the two kinds of Li_xAl foil

anodes against LFP cathodes. Comparison of electrochemical performance in Figure 3D shows that the LFP||S-Li_xAl pouch cell kept stable cycling for more than 70 cycles and exhibited significantly better performance than that of LFP||P-Li_xAl. Note that the unusual capacity fluctuation marked with the black box (Figure 4D) may be attributed to the temporarily electron and/or ionic or mechanical isolation, which made some capacity “quiescent.” However, with prolonged cycling, the huge volume expansion might reconnect the isolated parts and concomitantly activate the previously dead capacity. This seems to be a common phenomenon in the high-capacity anodes with large volume change, such as Si^[24] and Li^[25–27] anodes. However, the

fluctuation capacity is barely observed in LFP||S-Li_xAl full cells, since the improved electrochemical ductility helps the uniform phase transformation and volume change, and alleviates huge cracks to a large extent (see SEM images in Figure 5A–D).

We also used 4 V-class NCM523 cathode, which has a similar areal capacity ($\approx 2.4 \text{ mAh cm}^{-2}$) as the LFP cathode, as shown in Figure 4E,F. The stable voltage curves and long-term cycling performance with $\approx 80\%$ capacity retention after 160 cycles revealed good mutual compatibility. Even when paired against high-loading NCM523 (the areal capacity approaching 4 mAh cm^{-2}), the improved electrochemical ductility has facilitated NCM||S-Li_xAl full-cell to successfully double the cycling

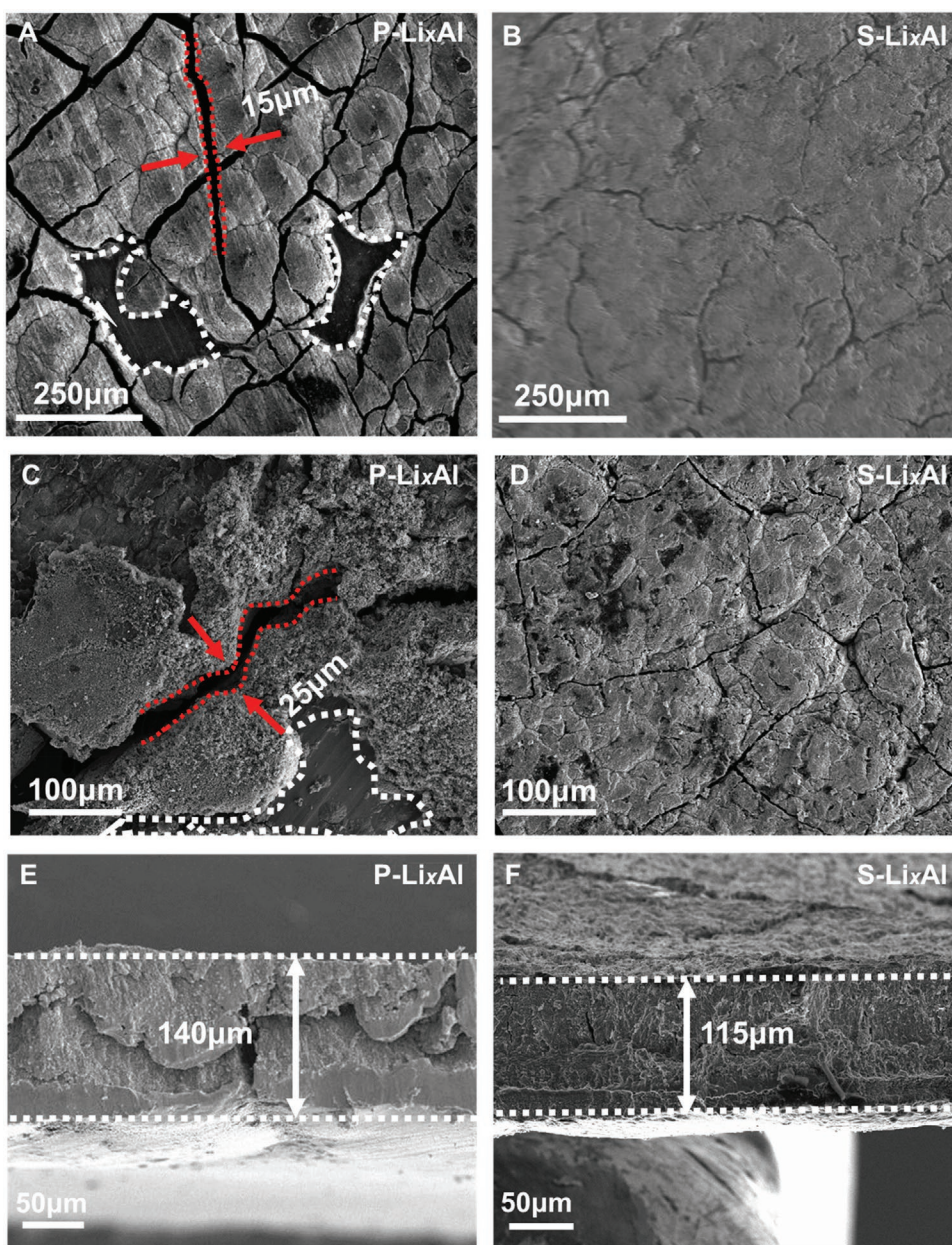


Figure 5. Postmortem examination of electrodes after cycling. A,B) SEM images of top-view of A) P-Li_xAl and B) S-Li_xAl electrodes after 20 cycles in the LFP||Li_xAl full cells, white dot line is marked as the EL area. C,D) Top-view of C) P-Li_xAl and D) S-Li_xAl electrodes after 50 cycles, white dot line is marked as the EL area. E,F) Cross-section images of E) P-Li_xAl foil and F) S-Li_xAl foil after 20 cycles.

life of NCM||P-Li_xAl (Figure S8D, Supporting Information). Additionally, the free-standing Li_xAl foil demonstrated wide tunability in terms of high-energy density, when thinner two-sided S-Li_xAl foils prepared by pressing 75 μm thick Al foils and 50 μm thick Li foils together were paired against high-loading LiCoO₂ cathodes (LCO, areal capacity ≈4.0 mAh cm⁻²), the gravimetric and volumetric energy density of as-assembled pouch cell (4 cm × 3.7 cm, Figure S9A, Supporting Information) were calculated to be 286 Wh kg⁻¹ and 706 Wh L⁻¹, respectively, based on the charging–discharging profiles in Figure S9B in the Supporting Information and weight/volumetric of each component in Figure S9C,D in the Supporting Information, which is quite competitive against commercial LIBs.^[28]

As a variation on the popular Li_{BCC} foil with anode-side LiInv, Li_xAl foil could also work well with conversion-type Li-free cathodes such as sulfur (S₈). As shown in Figure S10A in the Supporting Information, both the discharge capacity and CE maintained steady in S-Li_xAl||sulfur full cell, and the discharge capacity stabilizes at an acceptable value of ≈0.8 mAh cm⁻² in the initial 50 cycles. From the voltage profile in Figure S10B in the Supporting Information, the S-Li_xAl||sulfur battery is shown to work normally as the classic Li_{BCC}||sulfur battery, even though the voltage plateau is ≈0.25 V lower than that of Li_{BCC}||sulfur batteries, with the benefit of inhibiting Li_{BCC} dendrites with improved safety characteristics. Therefore, S-Li_xAl is highly competitive against pure Li metal foils in its intended range of applications.

To comprehensively understand the discrepancy in electrochemical performance between LFP||P-Li_xAl/S-Li_xAl full cells, postmortem examination of the electrodes after cycling was conducted. It is quite evident in Figure 5A that cracks have evolved to ≈15 μm wide in 20 cycles from the original ≈10 μm, and grew deeply into the P-Li_xAl electrode, reflecting the damage caused by the enormous unrelieved cyclic stresses. Conspicuous propagation of cracks and insufficient electrochemical ductility of P-Li_xAl are apparent, despite the excellent mechanical ductility of FCC P-Al. Even worse, cracks trigger positive feedback loop of electrolyte localization (EL), in which the liquid electrolyte (see the Experimental Section) preferentially flows into intergranular opening, and concentrates further phase transformations there, drying out the other regions.^[18] The EL-induced morphology is evident after 50 cycles with P-Li_xAl, as shown in Figure 5C. With EL, the P-Li_xAl generates even wider opening cracks (≈25 μm wide) and worse EL, cutting off large chunks of the active material from access to free electrons or ions. Finally, electronic percolation is lost due to large amount of “flotsam” entirely surrounded by electronically insulating SEI (Figure 5C). The conjoined problems of losing cyclable Li (LiInv), liquid electrolyte dry-out and unequal distribution that affect state-of-health of ionic percolation (SOHi) as well as losing electronic percolation (SOHe), all due to stress-corrosion cracking (SCC), show up more quickly in a full-cell test, and thus lead to terrible cliff-like decline in cycling performance. In striking contrast, the S-Li_xAl anode with originally smaller grain sizes before MP shows the neat and flat surface with much narrower and shallower micro-cracks, without any signs of EL after 20 cycles, in Figure 5B. The more robust structural stability of S-Li_xAl is also directly reflected in the electrochemical impedance spectroscopy (EIS) curves (Figure S11, Supporting Information). In

spite of the dramatic intrinsic volume change of phase transformation, the S-Li_xAl anode with a denser GB sliding system maintained integrity of the electrode after 50 cycles, showing reduced stress-corrosion cracking. Electrochemical ductility can thus be more specifically defined as the resistance of a high-capacity electrode against SCC during electrochemical cycling, to maintain electronic percolation (SOHe) and ionic percolation (SOHi), and sufficient anode-side plus cathode-side lithium inventory (LiInv) for future electrochemically throttled solid-state phase transitions (Figure 5D). This enhanced electrochemical ductility by shot-peening treatment, through which stress was released by GB sliding, effectively mitigated stress-corrosion cracking, delayed EL, and suppressed several-to-tens-of-micrometers-wide cracks and dead particles/flotsams. Except for the significant differences in surface topography, the cross-section also shows very different morphologies (Figure 5E,F), in which huge cracks of P-Li_xAl almost divide the electrode into two layers with loosened inner structure, almost like horizontal hydraulic fractures, while the S-Li_xAl is much denser and compact. Correspondingly, the nominal anode thickness increase is also significantly smaller than that of P-Li_xAl in cycling, indicating less porosity and SEI debris accumulation. Therefore, it can be reasonably concluded that the abundant GBs of S-Li_xAl electrode work analogously to using higher volume fraction of conductive binders^[29] in conventional LIB electrodes, underlying the good electrochemical ductility for better long-term cycling.

While anode prelithiation is a common strategy to counter ICE and loss of LiInv during cycling, as lithium metal foil and/or prelithiated graphite must be handled in moisture-controlled environment, prelithiation often greatly increases the manufacturing cost. The air stability of electrode materials is extremely important and cost-wise for the battery industry. Therefore, we measured the air stability of our prelithiated metallic alloy foils by exposing as-obtained S-Li_xAl foil to ambient air for 6, 12, 24 h with 20–30% relative humidity. As shown in Figure 6A, the electrochemically extractable LiInv decreases slowly with exposure time, and still maintained ≈83% (4.15 mAh cm⁻²) of its original capacity after 24 h. However, the P-Li_xAl shows less active LiInv than the S-Li_xAl foil after the same exposure time (Figure S12A, Supporting Information), which is mainly attributed to the larger number of initial cracks and porous structure of P-Li_xAl foil (≈32 vol% porosity), making it exposed much more surface to form the irreversible Li-Al-O phase in ambient air. Compared with the darkened Li foil, the S-Li_xAl foil shows only slight change in color after 24 h exposure (Figure 6B). The air stability of S-Li_xAl foil is related to its largely intact structure (Figure 3G) and the compact oxide film containing Al₂O₃. A post-mortem characterization was performed after exposing MPed S-Li_xAl foil in environments of 20–30% relative humidity, by comparing with its pure Li_{BCC} counterpart, as shown in Figure 6C,D. The original 100% dense Li_{BCC} foil demonstrated extensive deep cracking, just due to the air exposure and oxidation. Since Li₂O shrinks in volume compared to Li_{BCC}, with a Pilling–Bedworth ratio of $R_{PB}(Li_{BCC} \rightarrow Li_2O) = 0.567$, tensile stress will result from the oxidation, thus the tendencies to crack. Even worse, because Li₂O is hygroscopic, it will attract moisture in the environment, which is corrosive to Li_{BCC} instead of protective, making the oxidation of pure Li_{BCC}

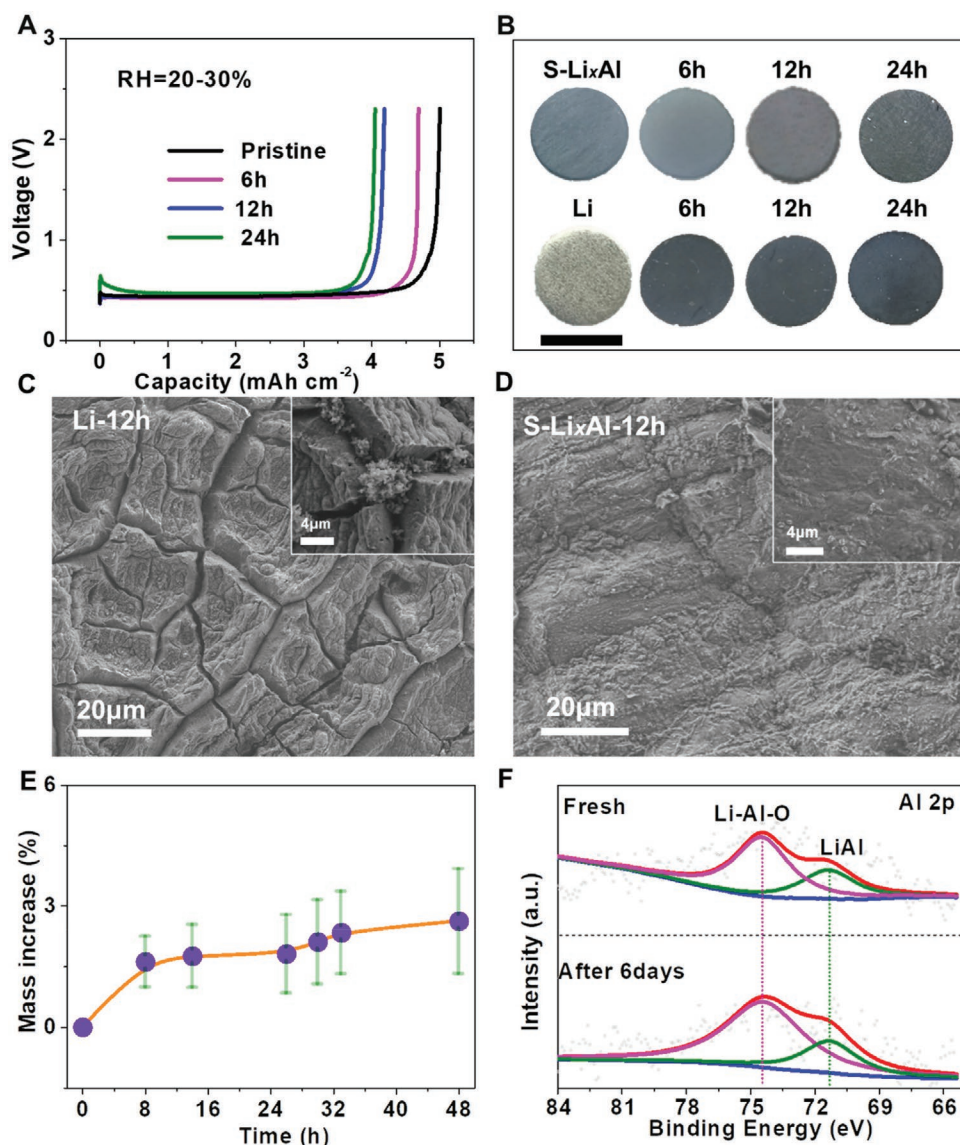


Figure 6. Air stability of S- Li_xAl . A) The capacity retention of S- Li_xAl foil after exposed to air for 6–24 h. B) Photographs of S- Li_xAl foil and fresh Li foil exposed to air after different time, scale bar is 1 cm. C,D) Surface tomography of C) Li foil and D) S- Li_xAl foil after 12 h exposure. E) The mass gain percentage of $\phi 12$ mm Li_xAl disks after various air-exposure time. F) XPS spectra of fresh and 6 days exposure Li_xAl foil.

a stress-corrosion cracking problem also (if $\text{Li}_{\text{BCC}} \rightarrow \text{LiOH}$, the Pilling–Bedworth ratio changes to $R_{\text{PB}}(\text{Li}_{\text{BCC}} \rightarrow \text{LiOH}) = 1.41$ instead, so there can be a whiplash effect). The nonpassivated oxidation of pure Li_{BCC} further deepened along these cracks, rendering complete oxidation of the entire foil eventually, like a dried-up creek bed. Not surprisingly, the case is totally different for the S- Li_xAl foil, which kept an intact morphology after the same exposure, with no microcracks observed even under large SEM magnification, as shown in Figure 6D. In order to investigate the oxidation process of Li_xAl foil, the mass gain percentage of $\phi 12$ mm Li_xAl disks after various air-exposure time was monitored, as shown in Figure 6E. An obvious $\approx 1.5\%$ weight gain in the first 10 h exposure, and afterward the mass increase rate slows down, to almost flat at 48 h. Moreover, the corresponding normalized XRD patterns of Li_xAl foil in Figure S12B in the Supporting Information demonstrated that

the LiAl still maintains the dominant phase even after 6 days exposure, despite a slight amount of Li_2CO_3 was generated. By contrast, the Li foil has been completely oxidized to the LiOH without any Li_{BCC} phase left only after 18 h exposure to ambient air (Figure S12C, Supporting Information). Therefore, it is reasonable to speculate an effective passivation layer is formed on the Li_xAl surface so as to prevent further corrosion in moist air. Such speculation gets verified by postmortem XPS examination in Figure 6F, where some Li-Al-O compounds were detected in the Al2P spectra of fresh (prepared in dry room) and 6-day-exposure samples, all accompanied by the LiAl peak as well. Note that once the exposure time exceeds 24 h, no more lithium could be extracted from Li_xAl disks in battery cells, but one can observe quite an intense reaction when putting the Li_xAl disks in water, indicating the compact and ionically insulating Li-Al-O layer prevented the LiInv being electrochemically active.

Interestingly, the reaction in water lasts for 8 min (Figure S12D and Video S1, Supporting Information), much longer than the fresh Li_xAl counterpart, which usually violently reacts in 60 s. Such an observation also implies the continuous protection for the active LiInv by the compact Li-Al-O film in air.

In summary, we defined the concept of electrochemical ductility and distinguished it from mechanical ductility. We found the invasion of Li atoms into Al matrix is preferentially along the GBs and the phase transformation would also happen locally there, and we argued that “electrochemical ductility” of such high-capacity conversion/alloying electrodes should be based on grain boundary activities such as GB sliding, especially when dealing with cyclic phase transformations in metallic alloy foils, in order to maintain the grain-to-grain adhesion in battery cycling. Based on this understanding, we developed a facile roll-to-roll metallurgical prelithiation technique, combined with a shot-peening treatment for electrochemical ductility enhancement. Our analysis indicated that with more prolific GB sliding systems to release residual stresses, less stress was transmitted across GB that abets stress corrosion cracking (SCC), and the refined-grained foil by shot-peening treatment demonstrated less initial damage after MP, whose porosity after MP shock decreased from 31.4% to 17.1%. When pairing the copper current collector-free and binder-free S- Li_xAl foil anode against NCM cathodes, the full cell could maintain stable cycling for 160 cycles, and pouch cells using LiFePO_4 cathodes also exhibit decent performance. In addition, air stability is surprisingly robust with Li_xAl foil, with negligible capacity loss after several hours' exposure in moist air. The durabilities of thin S- Li_xAl foil against stress-corrosion cracking in diverse environments from organic electrolytes to moist air with complex phase-transformation generated stresses and grain-to-grain incompatibilities illustrate that it indeed has superior electrochemical ductility. This greatly boosts the practical applicability of thin Al foil anodes from a curiosity to pouch full cells with competitive performance against heavily optimized industrial LIBs, and provides mechanistic insights into further improvements of these metallic foil anodes which could be highly competitive against pure Li_{BCC} foils.

3. Experimental Section

Preparation of Shot-Peening Al Foil: High-purity Al foil (99.99%, 40 mm × 40 mm) was washed with acetone, distilled water, and absolute ethanol to remove the surface oil pollution and impurities, and then dried in the oven. The shot-peening process employed an average diameter of 0.74 mm glass projectile (BZ), and the pressure was 1.2 bar.

Preparation of Li_xAl Foil: For the roll-to-roll prelithiation of the Al foil anode, a piece of 10 cm × 5 cm × 50 μm Li foil (China Energy Lithium Co., Ltd.) and two pieces of 12 cm × 5 cm × (40–100) μm Al foil were stacked together and rolled with a roller (MSK-2150, Shenzhen Kejing Star Technology, Ltd) in air at 30 MPa pressure.

Characterization: The morphologies and structures of Li_xAl foil were determined by a field-emission SEM (FEI, QUANTA 250FEG) under an accelerate voltage of 10 kV. XRD measurements were carried out on a Bruker D8-Advance powder X-ray diffractometer operating at 40 kV and 30 mA, using Cu K α radiation ($\lambda = 0.15405$ nm). The TEM (FEI Talos F200) was performed to determine the grain size on both pristine Al foil and S-Al foil. The EBSD characterization was carried out at acceleration voltage of 20 kV with a beam current of 17 nA (NordlysF+, Shanghai Oxford Instruments Co., Ltd.). CV and EIS measurements

were performed on an electrochemical work station (CHI660E, Shanghai Chen Hua Instrument Co., Ltd.).

Electrochemical Cycling Tests: Al foils (40–100 μm, 99.99%) were punched into disks with a diameter of 12 mm; the commercial LiFePO_4 with a capacity of 2.65 mAh cm⁻² with 12 mm diameter were used as cathode in full cells. The commercial $\text{LiNi}_{0.5}\text{Co}_{0.2}\text{Mn}_{0.3}\text{O}_2$ (NCM) with a diameter of 12 mm was used as cathode in NCM|| Li_xAl full-cell. 40 μL of 1 M lithium hexafluorophosphate (LiPF₆) in a 1:1 vol/vol mixture of ethylene carbonate and diethyl carbonate with 10 wt% fluorinated ethylene carbonate and 1 wt% vinylene carbonate was used as electrolyte. High-voltage electrolyte (bought from Dodochem) was used for NCM|| Li_xAl full-cell. Li_xAl ||S battery was test in the ether-based electrolyte (1,3-dioxolane and 1,2-dimethoxyethane (volume ratio: 1:1) with 2 wt% LiNO_3 as additive).

All the coin cells were assembled in the CR2025-type coin cells, and the electrochemical performance of cells were carried out by Neware test system (CT-4008, Neware). The Al||Li half cells were delithiated to 2.3 V. The LFP|| Li_xAl full cells were examined between 2.0 and 4.0 V. The electrochemical test on NCM|| Li_xAl full-cells was carried out between 2.5 and 4.2 V. Li_xAl ||S battery was test between 1.5 and 2.5 V. The double-sided lithiated Al foils (initial thickness is 93 μm) and two pieces of commercial LiFePO_4 (≈ 2.65 mAh cm⁻², 3 cm × 3 cm) were used as anode in the pouch cell. The Li_xAl || LiCoO_2 pouch cells were assembled with double-sided lithiated Al foils (initial thickness is 75 μm) and two pieces of commercial LiCoO_2 (≈ 4 mAh cm⁻², 3.7 cm × 4 cm).

Supporting Information

Supporting Information is available from the Wiley Online Library or from the author.

Acknowledgements

The authors are grateful for the support from Tongji University and the National Natural Science Foundation of China (NSFC-No. 91934303, 51602222, and 51632001). J.L. acknowledges the support by Samsung Advanced Institute of Technology.

Conflict of Interest

The authors declare no conflict of interest.

Data Availability Statement

Research data are not shared.

Keywords

air stable, mechanical prelithiation, phase transformation, shot peening, stress corrosion cracking

Received: January 29, 2021

Revised: March 25, 2021

Published online: May 3, 2021

[1] F. Zhang, B. Ji, X. Tong, M. Sheng, X. Zhang, C.-S. Lee, Y. Tang, *Adv. Mater. Interfaces* **2016**, *3*, 1600605.

[2] S. Li, J. Niu, Y. C. Zhao, K. P. So, C. Wang, C. A. Wang, J. Li, *Nat. Commun.* **2015**, *6*, 7872.

- [3] B. Ji, F. Zhang, M. Sheng, X. Tong, Y. Tang, *Adv. Mater.* **2017**, *29*, 1604219.
- [4] W. Meng, Z. Fan, C. S. Lee, Y. Tang, *Adv. Energy Mater.* **2017**, *7*, 1602582.
- [5] X. Tong, F. Zhang, B. Ji, M. Sheng, Y. Tang, *Adv. Mater.* **2016**, *28*, 9979.
- [6] H. Xu, S. Li, X. Chen, C. Zhang, W. Liu, H. Fan, Y. Yu, Y. Huang, J. Li, *Adv. Energy Mater.* **2019**, *9*, 1902150.
- [7] Y. Yu, S. Li, H. Fan, H. Xu, M. Jiang, Y. Huang, J. Li, *Nano Energy* **2019**, *67*, 104274.
- [8] H. Xu, S. Li, X. Chen, C. Zhang, Z. Tang, H. Fan, Y. Yu, W. Liu, N. Liang, Y. Huang, J. Li, *Nano Energy* **2020**, *74*, 104815.
- [9] H. Xu, S. Li, C. Zhang, X. Chen, W. Liu, Y. Zheng, Y. Xie, Y. Huang, J. Li, *Energy Environ. Sci.* **2019**, *12*, 2991.
- [10] Y. Jin, S. Li, A. Kushima, X. Zheng, Y. Sun, J. Xie, J. Sun, W. Xue, G. Zhou, J. Wu, F. Shi, R. Zhang, Z. Zhu, K. So, Y. Cui, J. Li, *Energy Environ. Sci.* **2017**, *10*, 580.
- [11] H. M. Fan, B. Chen, S. Li, Y. Yu, H. Xu, M. W. Jiang, Y. H. Huang, J. Li, *Nano Lett.* **2020**, *20*, 896.
- [12] A. Ishii, J. Li, S. Ogata, *Int. J. Plast.* **2016**, *82*, 32.
- [13] D. Trinkle, R. Hennig, S. Srivilliputhur, D. Hatch, M. Jones, H. Stokes, R. Albers, J. Wilkins, *Phys. Rev. Lett.* **2003**, *91*, 025701.
- [14] J. W. Christian, *The Theory of Transformations in Metals and Alloys*, Pergamon, Oxford/New York **2002**.
- [15] S. Han, J. Park, W. Lu, A. M. Sastry, *J. Power Sources* **2013**, *240*, 155.
- [16] S. Yang, B. Yan, T. Li, J. Zhu, L. Lu, K. Zeng, *Phys. Chem. Chem. Phys.* **2015**, *17*, 22235.
- [17] A. G. Evans, *J. Am. Ceram. Soc.* **1990**, *73*, 187.
- [18] M. Jjiang, Y. Yu, H. Fan, H. Xu, Y. Zheng, Y. Huang, S. Li, J. Li, *ACS Appl. Mater. Interfaces* **2019**, *11*, 15656.
- [19] Y.-S. Nam, Y.-I. Jeong, B.-C. Shin, J.-H. Byun, *Mater. Des.* **2015**, *83*, 566.
- [20] J. González, S. Bagherifard, M. Guagliano, I. F. Pariente, *Eng. Fract. Mech.* **2017**, *185*, 72.
- [21] Y. G. Liu, M. Q. Li, H. J. Liu, *J. Alloys Compd.* **2016**, *685*, 186.
- [22] L.-F. Hou, Y.-H. Wei, X.-F. Shu, B.-S. Xu, *J. Alloys Compd.* **2010**, *492*, 347.
- [23] S. Li, M. Jiang, Y. Xie, H. Xu, J. Jia, J. Li, *Adv. Mater.* **2018**, *30*, 1706375.
- [24] M. J. Loveridge, M. J. Lain, I. D. Johnson, A. Roberts, S. D. Beattie, R. Dashwood, J. A. Darr, R. Bhagat, *Sci. Rep.* **2016**, *6*, 37787.
- [25] Q. Ma, X. Zhang, A. Wang, Y. Xia, X. Liu, J. Luo, *Adv. Funct. Mater.* **2020**, *30*, 2002824.
- [26] Y. Zhu, Y. Han, H. Wang, Q. Guo, H. Jiang, W. Sun, W. Xie, C. Zheng, K. Xie, *Ionics* **2020**, *26*, 3307.
- [27] J.-S. Kim, H. Choi, J.-N. Lee, H. Kang, D. Im, H. Kim, *RSC Adv.* **2017**, *7*, 24679.
- [28] E. J. Berg, C. Villevieille, D. Streich, S. Trabesinger, P. Novák, *J. Electrochem. Soc.* **2015**, *162*, A2468.
- [29] G. Xu, Q.-B. Yan, A. Kushima, X. Zhang, J. Pan, J. Li, *Nano Energy* **2017**, *31*, 568.

ADVANCED FUNCTIONAL MATERIALS

Supporting Information

for *Adv. Funct. Mater.*, DOI: 10.1002/adfm.202100978

Air-Stable Li_xAl Foil as Free-Standing Electrode with Improved Electrochemical Ductility by Shot-Peening Treatment

Huimin Fan, Sa Li, Yue Yu, Hui Xu, Mengwen Jiang, Yunhui Huang, and Ju Li*

Supporting Information

Air-stable Li_xAl foil as free-standing electrode with improved electrochemical ductility by shot-peening treatment

Huimin Fan^{1,2}, Sa Li^{1,2*}, Yue Yu^{1,2}, Hui Xu^{1,2}, Mengwen Jiang^{1,2}, Yunhui Huang^{1,2} and Ju Li³

¹School of Materials Science and Engineering, Tongji University, Shanghai 201804, China

²Institute of New Energy for Vehicles, Tongji University, Shanghai 201804, China

³Department of Nuclear Science and Engineering and Department of Materials Science and Engineering, Massachusetts Institute of Technology, Cambridge, MA 02139, USA

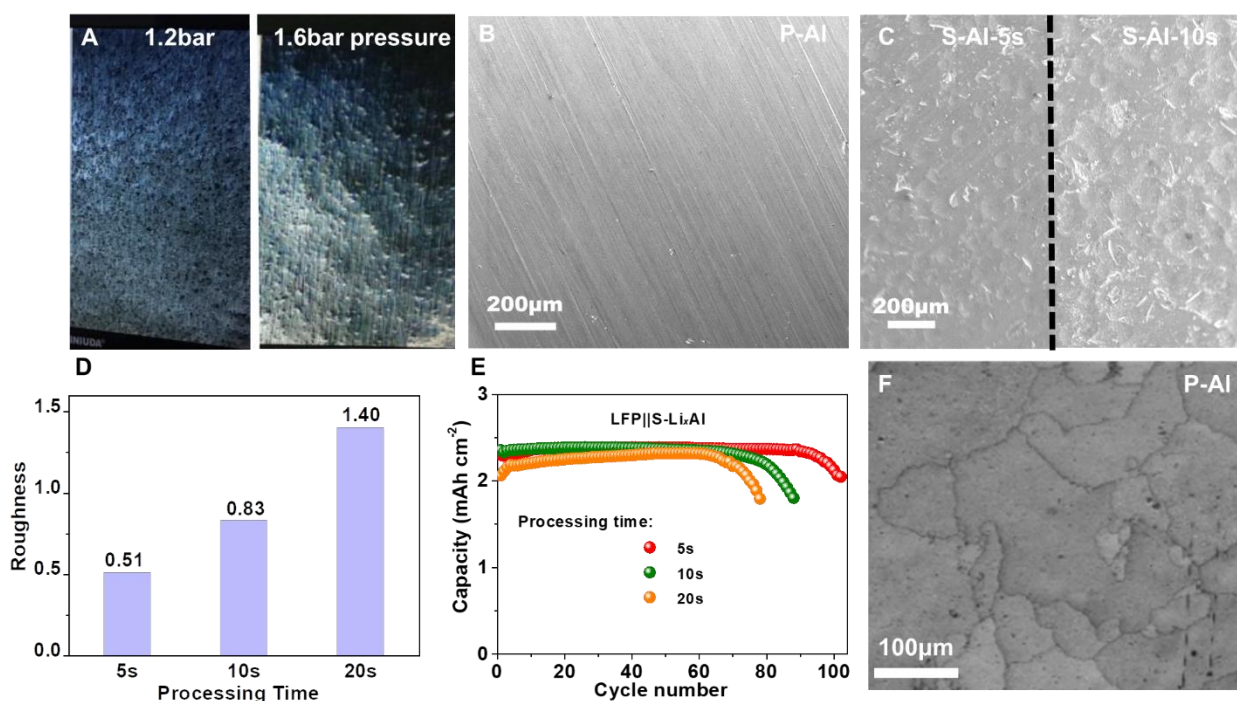


Figure S1. (A) Optical photo collected from the shot peening Al foil in the pressure of 1.2 and 1.6 bar. (B-C) SEM images of surface morphology collected from P-Al and S-Al foil for 5s and 10s. (D) Surface roughness of the different treated Al foil. (E) Electrochemical performance comparison of various kinds of Li_xAl foil paired against LFP cathodes with different Li_xAl foils with various shot peening processing time. (F) Band contrast map of EBSD data collected from P-Al foil.

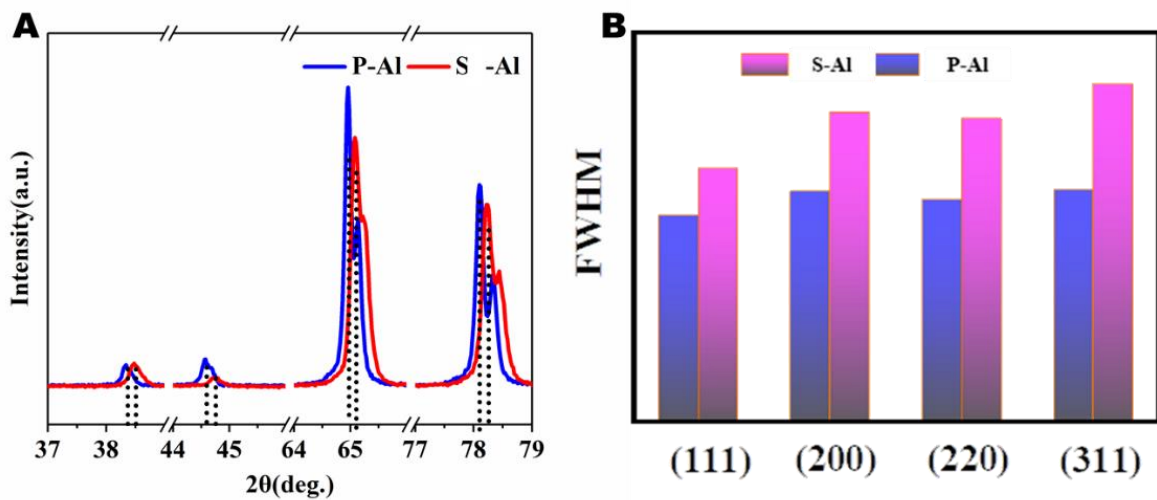


Figure S2. (A) Detail XRD patterns for P-Al and S-Al. (B) Rough comparison of full width at half maximum (FWHM) of S-Al and P-Al.

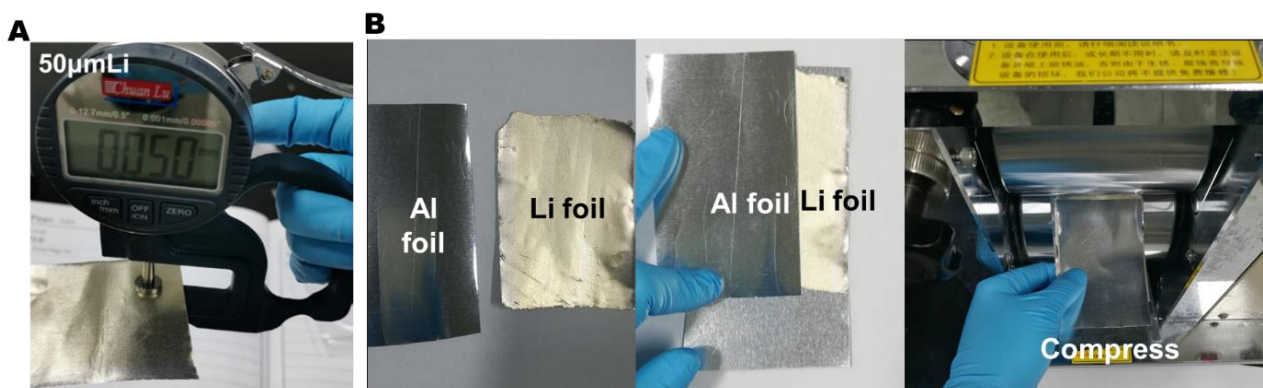


Figure S3. (A) Optical photographs of 50- μm -thick Li foil. (B) Operation procedure of practical operation in the laboratory.

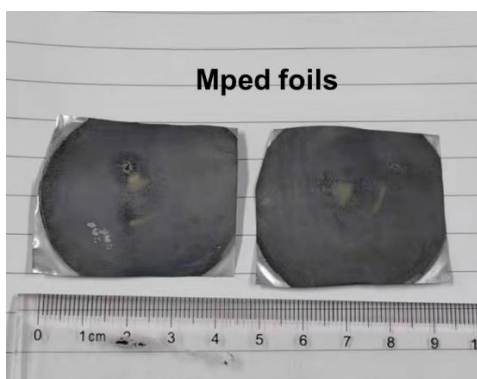


Figure S4. Photographs of Li_xAl foil after roll-to-roll lithiation.

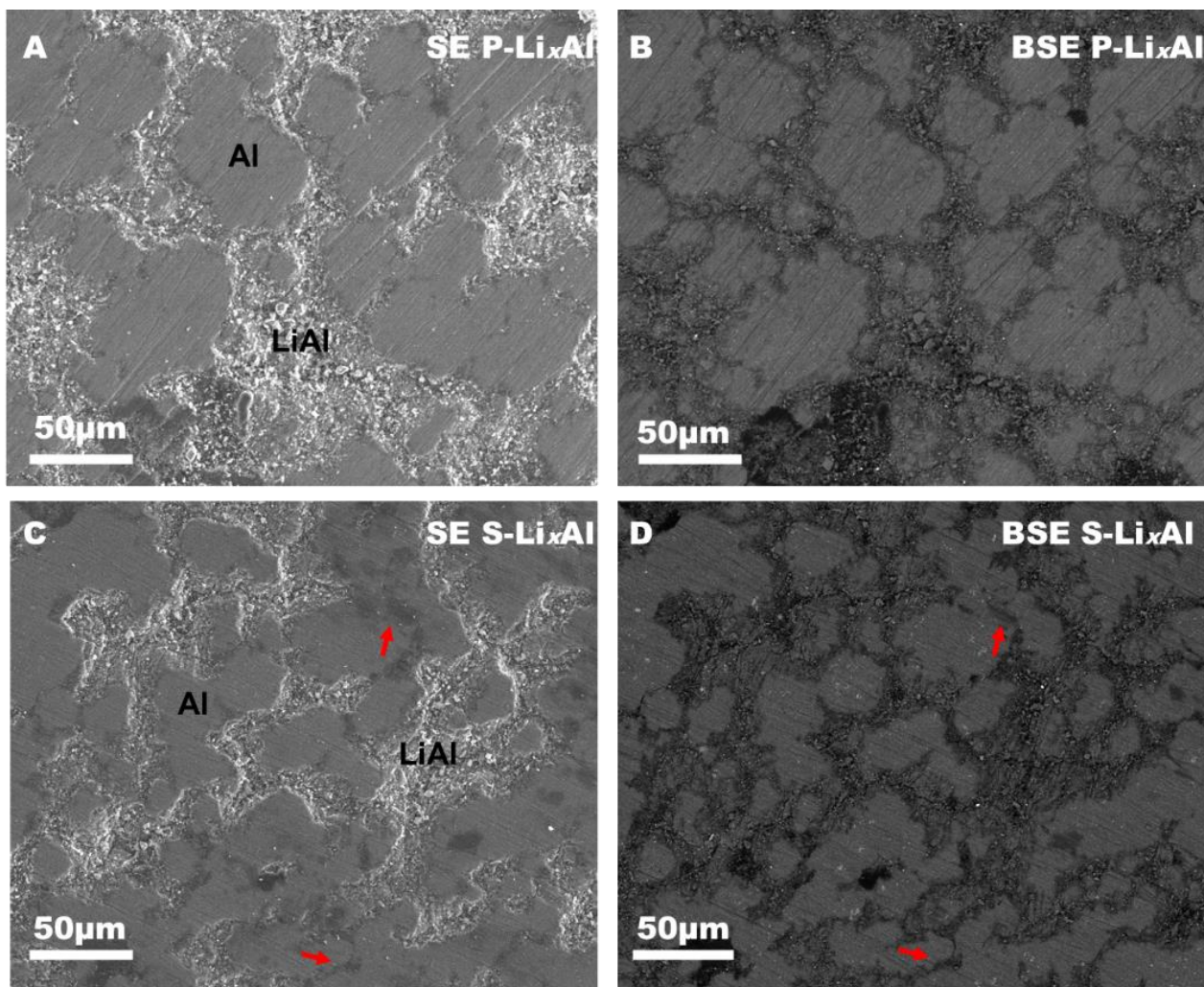


Figure S5. (A) Secondary electron (SE) signals of P-Li_xAl samples; (B) Back scattered electron signals (BSE) of P-Li_xAl sample (C and D) SE and BSE mode of S-Li_xAl sample, respectively.

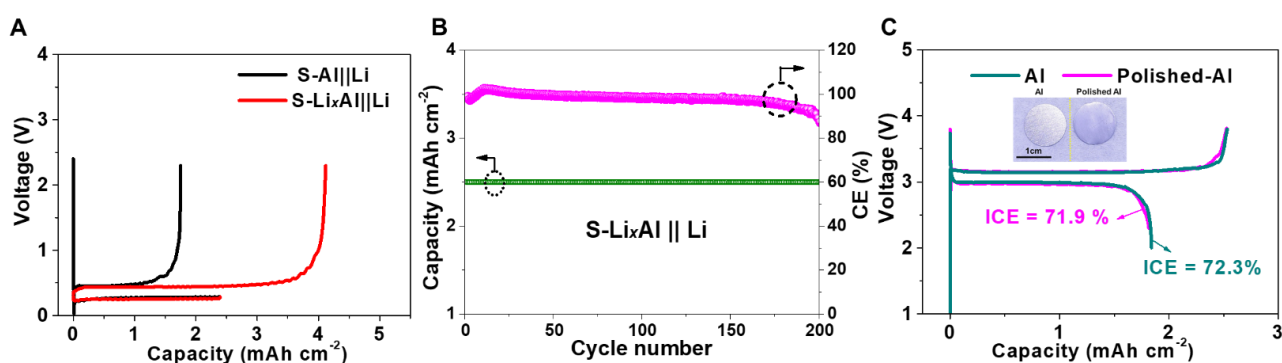


Figure S6. (A) Initial voltage comparison of the S-Al||Li, S-Li_xAl||Li half cells. (S-Li_xAl anode was firstly lithiated with 2.5 mAh cm⁻² and then was delithiated to a cut-off voltage of 2.3 V) (B) Half-cell performance of the S-Li_xAl||Li cells. (C) Initial voltage profiles of pure Al in LFP full cells before and after polishing the Alumina in Ar glove-box.

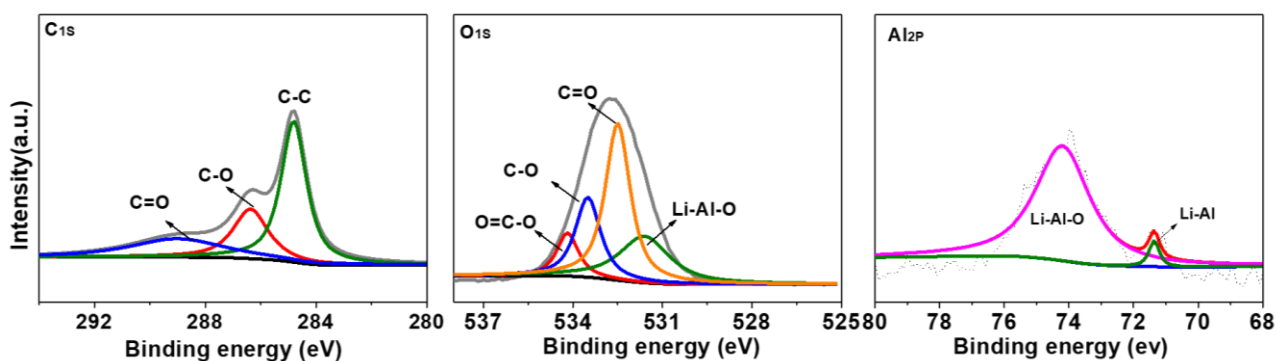


Figure S7. XPS analysis of Li_xAl anode after cycles.

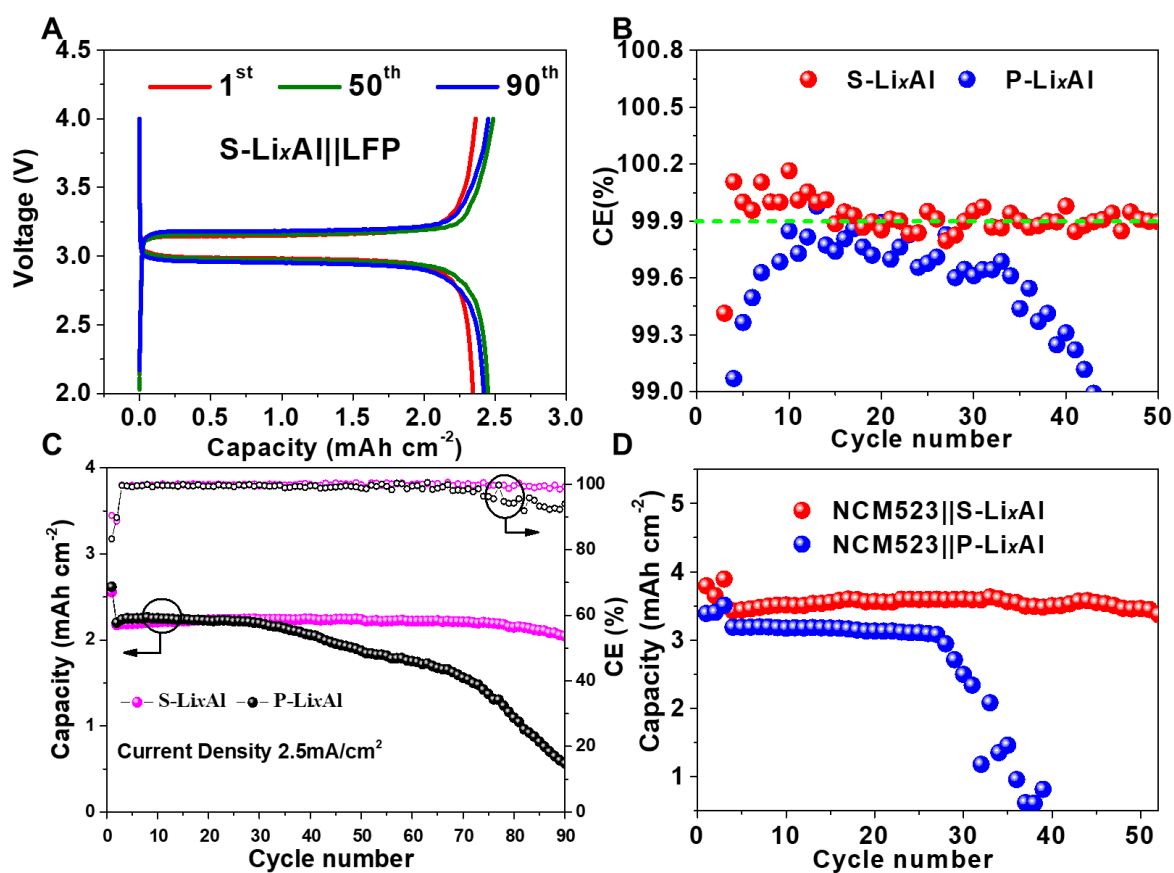


Figure S8. (A) Voltage profiles of $\text{S-Li}_x\text{Al}||\text{LFP}$ upon cycling. (B) CE comparison between $\text{S-Li}_x\text{Al}||\text{LFP}$ and $\text{P-Li}_x\text{Al}||\text{LFP}$ full cells. (C) Cycling performance comparison at 2.5 mA cm^{-2} (1C) with LFP cathodes in full cells. (D) Electrochemical stability with high-voltage and high-loading NCM cathodes.

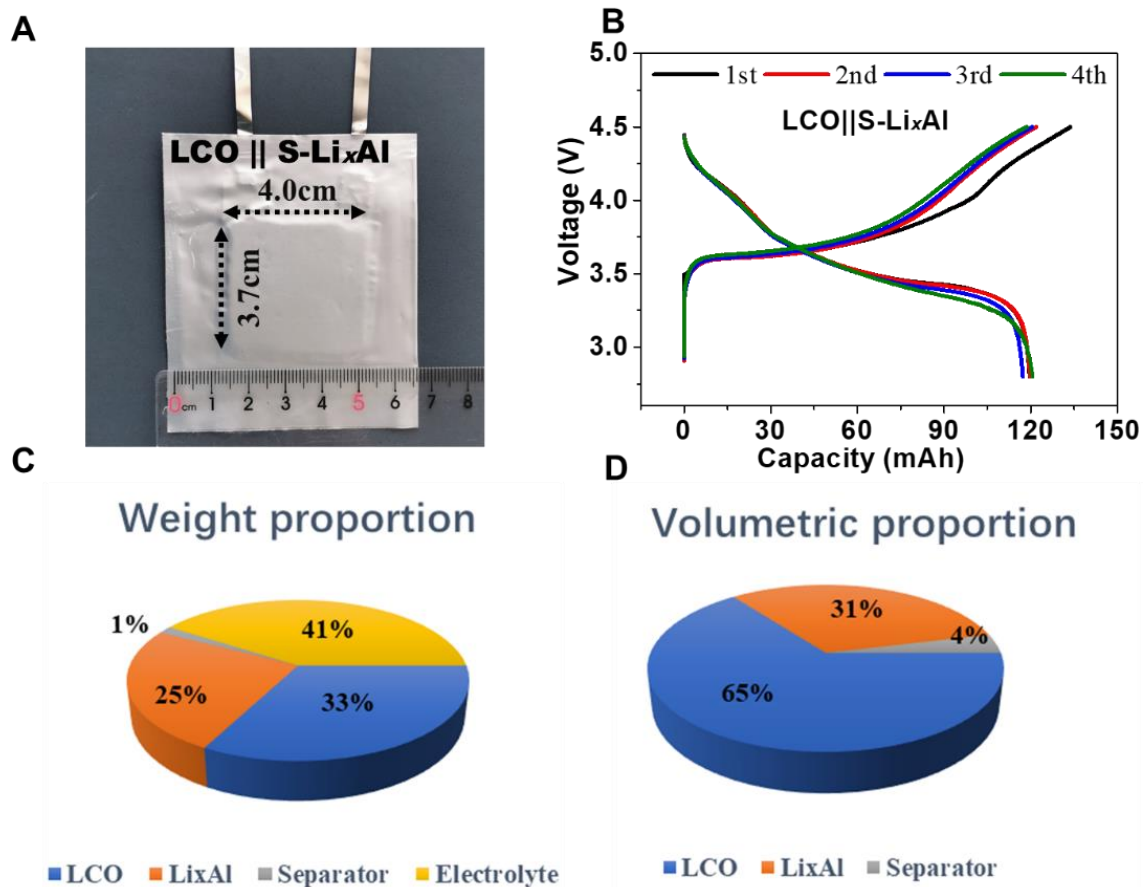


Figure S9. (A) Corresponding Optical photograph of LCO||S-Li_xAl pouch cell. (B) Voltage curves of LCO||S-Li_xAl pouch cell at the initial few cycles. (C-D) Weight and volumetric percentage of each component for the pouch cell.

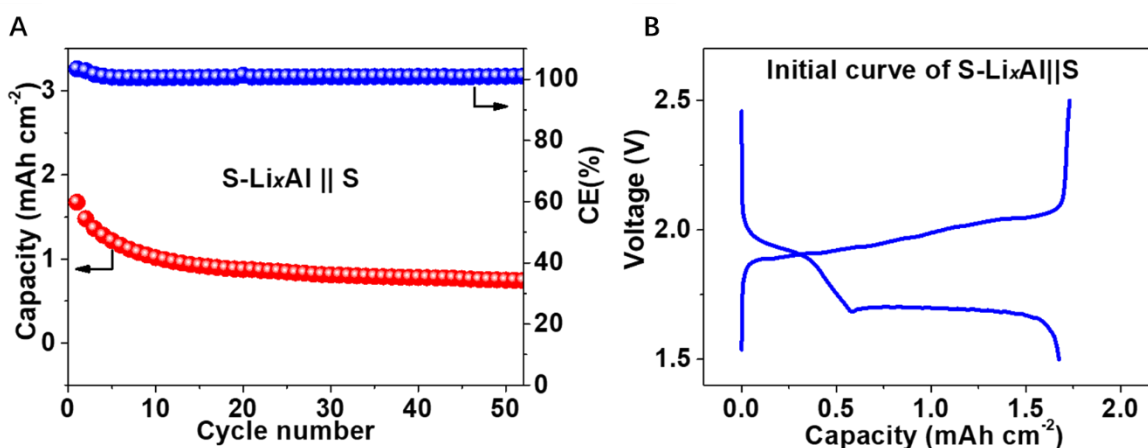


Figure S10. (A) S-Li_xAl||Sulfur battery performance in the ether-based electrolyte. (B) Initial voltage curve of the S-Li_xAl||Sulfur battery.

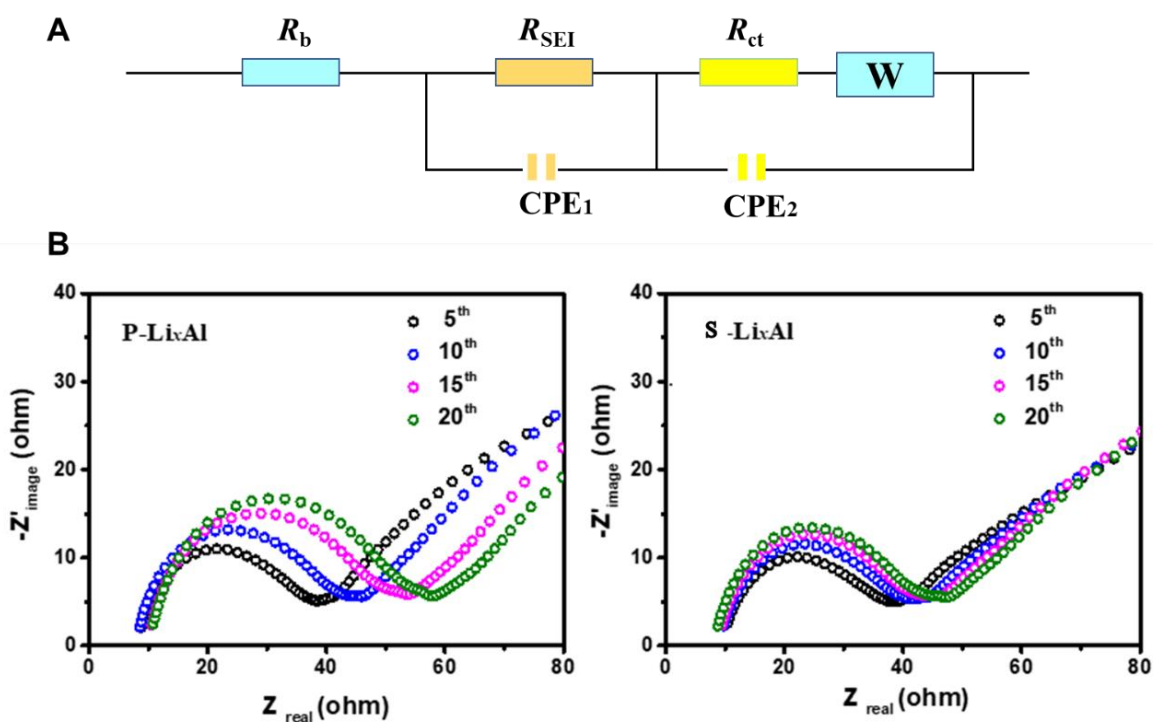


Figure S11. (A) The enlarged equivalent circuit diagram. (B) EIS plots of the two kinds of Li_xAl foil at different cycle number in full cells.

The EIS results fitted with equivalent circuit mode were shown in Figure S11a, in which the intercept in high-frequency is attributed to the bulk ohmic resistance, referred as R_b , and the semi-circle is attributed to the interfacial resistance (R_{SEI}) and charge transfer resistance (R_{ct}) respectively, and the CPE represents a constant phase element, W stands for a Warburg element.^{S[1]} Since the charge transfer involves Li alloying/dealloying process at the Li_xAl anode and intercalation/deintercalation process at the LFP cathode, the two processes might have similar frequency response, thus only single $R_{\text{ct}} // \text{CPE}_2$ module is applied to describe the charge transfer process. As the side reactions passivate the anode-electrolyte interphases with cycling, Li^+ transport pathway through the anode will be blocked and the available anode surface will reduce, enlarging both R_{SEI} and R_{ct} , consistent with the EIS analysis. But the interfacial impedance condition of S- Li_xAl is much better than that of the P- Li_xAl , suggesting it is easier to “mine” the lithium inventory embedded in S- Li_xAl benefited from the well-constructed structure.

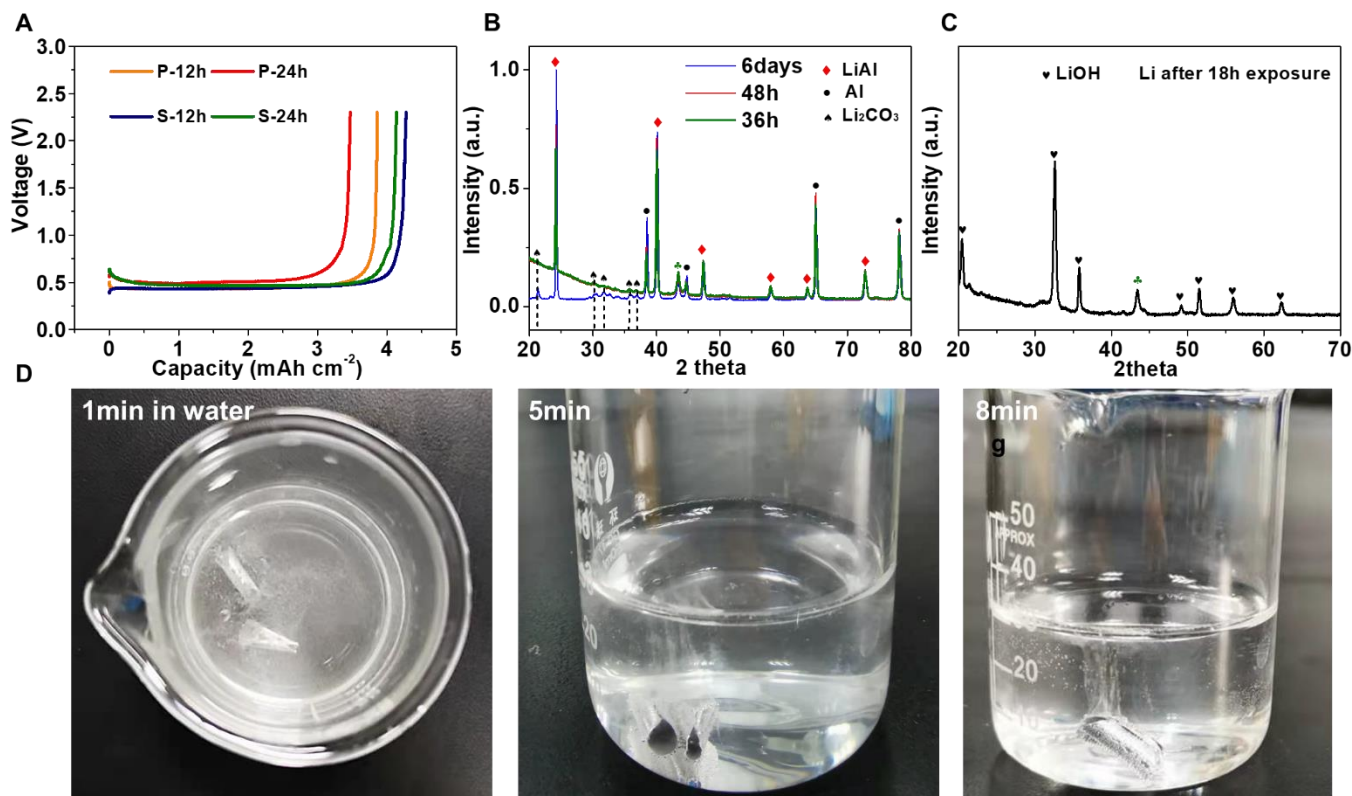


Figure S12. (A) Air-stability comparison between P-Li_xAl and S-Li_xAl foil. (B) XRD spectra of Li_xAl foil after 36h, 48h and 6-day exposure time. (C) XRD spectra of Li foil after 18h exposure. (D) Optical photo of Li_xAl foil after long time (> 48 h) exposure in water. (Note that the green mark at 43.6° in (B and C) belongs to XRD specimen stage)

Video S1: <http://li.mit.edu/S/HuiminFan/Upload/6043b230d86d6d63db9e8053bfb41235.mp4>

Supplementary note

Presuming no porosity is generated during MP, and no lateral expansion, the theoretical thickness is calculated. From *ab initio* calculations (materialsproject.org), Li_{BCC} (mp-135) has volume per Li atom of 20.121 \AA^3 , Al_{FCC} (mp-134) has volume per Al atom of 16.472 \AA^3 , and $\text{LiAl}_{\text{Cubic}}$ (mp-1067) has volume per LiAl of 32.103 \AA^3 , almost double that of Al_{FCC} and which is the basis for the shock. So to absorb 25 \mu m worth of Li_{BCC} , at least $(16.472/20.121) \times 25 \text{ \mu m} = \mathbf{20.47 \text{ \mu m}}$ worth of Al_{FCC} is needed for the reaction, forming $\mathbf{39.887 \text{ \mu m}}$ worth of $\text{LiAl}_{\text{Cubic}}$ and leaving $\mathbf{93-20.47=72.53 \text{ \mu m}}$ unreacted Al_{FCC} (as-received S-Al and P-Al foil is 93 \mu m thick). The ideal thickness of the S- Li_xAl and P- Li_xAl foils is supposed to be $39.887+72.53 = 112.4 \text{ \mu m}$ after the reaction, if no porosity and no lateral expansion are involved.

Then the actual apparent thicknesses of S- Li_xAl and P- Li_xAl samples are measured and shown in Table S1. The total apparent thickness is decomposed into the apparent reacted layer thickness and the unreacted layer thickness $t_{\text{total}} = t_{\text{react}} + t_{\text{unrea}}$. Independent measurements are performed at different locations of the foil to not only obtain the average $E[t]$, but also the standard deviation $\sigma[t]$ (the value behind the \pm in Table S2-5). Note that when measuring t_{react} and t_{unrea} , 20 random spots were selected (Figure S12). Additionally, however, we noticed that there is actually lateral areal expansion (Figure S13 and Table S6) during MP, meaning there can be sample-wide plastic deformation in both in-plane x, y and out-of-plane z . We therefore define:

$$\alpha \equiv \text{area (after MP)} / \text{area (before MP)} \quad (2)$$

and find $\alpha=1.21$ for P- Li_xAl , but is very close to 1.1 in S- Li_xAl (Table S6). We can then calculate the porosity within the apparent reacted layer:

$$p \equiv (E[t_{\text{total}}] - 112.4 \text{ \mu m} / \alpha) / E[t_{\text{react}}] \quad (3)$$

as the unreacted layer is clearly still fully dense, and find that $p_{\text{P-Li}_x\text{Al}} = 13.2 \text{ \mu m} / 42.1 \text{ \mu m} = \mathbf{31.4\text{vol\%}}$, which is a huge amount of porosity, approaching that of slurry coatings (even though we profess to make a foil anode). In contrast, $p_{\text{S-Li}_x\text{Al}} = 9.25 \text{ \mu m} / 53.9 \text{ \mu m} = \mathbf{17.1\text{vol\%}}$, which is much less damaging, considering not all free volume belong to open pores and much of the 17.1vol% could be trapped inside the ultra-nanocrystalline LiAl/LiAl GBs that facilitate Li GB diffusion but do not allow liquid electrolyte invasion.

Table S1. Measured thickness of all the samples.

Thickness (μm)	P-Al	S-Al	P- Li_xAl	S- Li_xAl
Total thickness (t_{total})	93	93	106.1	111.2
Reacted layer (t_{react})	--	--	42.1	53.9
Unreacted layer (t_{unrea})	--	--	64	57.3

Table S2. Reacted thickness (t_{react}) measurement result of the S- Li_xAl sample.

Thickness (μm) of the foil					Average thickness	Standard Deviation	Reacted thickness
56.3	54.4	52.5	52.5	54.9	53.9 μm	1.8 μm	53.9 \pm 1.8 μm
53.0	56.3	58.9	52.5	53.0			
53.0	54.2	52.5	54.9	51.3			
54.2	52.2	51.3	56.3	54.9			

Table S3. Thickness ($E[t_{total}]$) measurement result of the S- Li_xAl sample.

Thickness (μm) of the foil					Average thickness	Standard Deviation	Total thickness
112.2	112.2	111.5	111.1	113.9	111.2 μm	1.5 μm	111.2 \pm 1.5 μm
111.7	112.3	112.2	112.1	110.8			
112.1	108.4	107.7	109.3	112.1			
112.1	110.1	108.4	111.8	112.2			

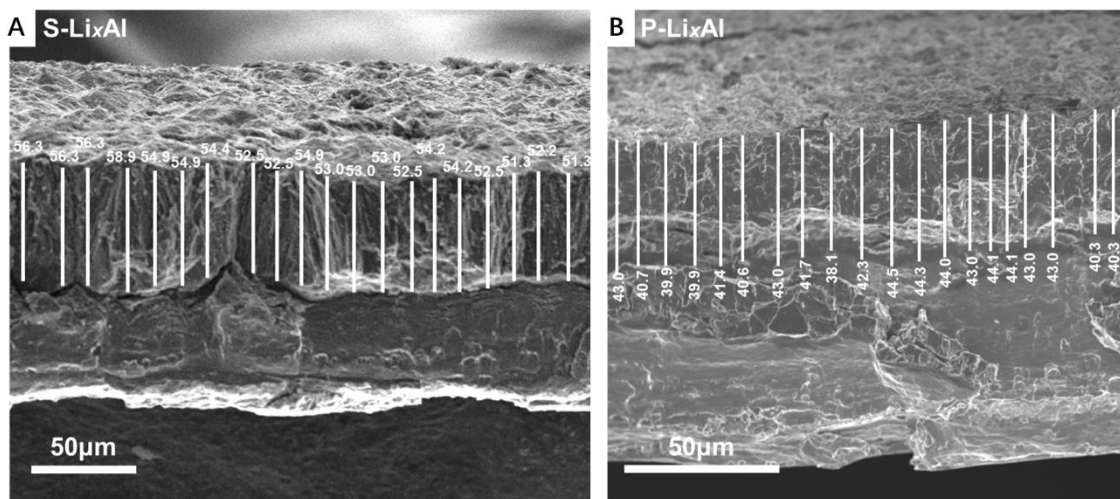


Figure S13. 20 random spots selected from S- Li_xAl (A) and P- Li_xAl (B) respectively.

Table S4. Reacted thickness (t_{react}) result of the P- Li_xAl sample.

Thickness (μm) of the foil					Average thickness	Standard Deviation	Reacted thickness
43.0	41.4	38.1	44.0	43.0	42.1 μm	1.8 μm	42.1 \pm 1.8 μm
40.4	40.6	42.3	43.0	40.3			
39.9	43.0	44.5	44.1	40.3			
39.9	41.7	44.3	43.0	44.1			

Table S5. Thickness ($E[t_{total}]$) measurement result of the P- Li_xAl sample.

Thickness (μm) of the foil					Average thickness	Standard Deviation	Total thickness
103.8	107.5	104.3	108.6	107.5	106.1 μm	1.93 μm	106.1 \pm 1.93 μm
104.3	104.8	102.1	107.5	107.3			
107.5	108.6	104.3	105.9	106.1			
105.8	105.4	103.5	107.3	109.4			

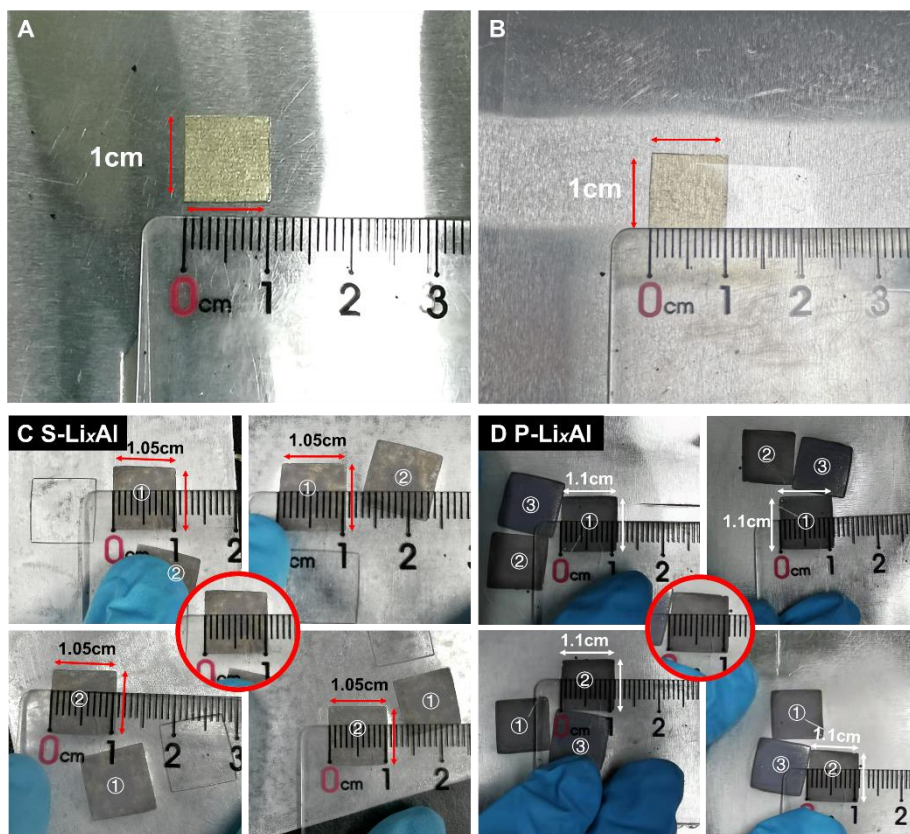


Figure S14. Lateral areal expansion measurement for S- Li_xAl and P- Li_xAl . (A-B) The pristine $1\text{cm} \times 1\text{cm}$ Li foil. (C) Measurement of the as-formed Li_xAl area on S-Al after MP. (D) Measurement of the as-formed Li_xAl area on P-Al after MP.

Table S6. Lateral areal expansion of the two samples after MP

Sample	S- Li_xAl	P- Li_xAl
Size of Li foil (before MP)	$1\text{ cm} \times 1\text{ cm}$	$1\text{ cm} \times 1\text{ cm}$
Size of Li_xAl area (after MP)	$1.05\text{ cm} \times 1.05\text{ cm}$	$1.1\text{ cm} \times 1.1\text{ cm}$
Lateral areal expansion	10%	21%
α	1.1	1.21

Reference

S[1]Y. X. Ren, T. S. Zhao, M. Liu, Y. K. Zeng, H. R. Jiang, *J. Power Sources* **2017**, 361, 203-210.